Journal of Inorganic and Organometallic Polymers and Materials (2020) 30:3626–3645
https://doi.org/10.1007/s10904-020-01560-3

Structural Refinement, Morphological Features, Optical Properties, and Adsorption Capacity of α-Ag_2WO_4 Nanocrystals/SBA-15 Mesoporous on Rhodamine B Dye

F. C. M. Silva[1] · L. K. R. Silva[1] · A. G. D. Santos[2] · V. P. S. Caldeira[2] · J. F. Cruz-Filho[3] · L. S. Cavalcante[3] · E. Longo[4] · G. E. Luz Jr.[1,3]

Received: 30 January 2020 / Accepted: 24 April 2020 / Published online: 2 May 2020
© Springer Science+Business Media, LLC, part of Springer Nature 2020

Abstract

α-Ag_2WO_4 nanocrystals, mesoporous silica (SBA-15), and α-Ag_2WO_4/SBA-15 as a nanocomposite were prepared by sonochemical, hydrothermal, and in situ sonochemical methods respectively. Samples were characterized by X-ray diffraction (XRD), Rietveld refinement, micro-Raman, Fourier-transform infrared spectroscopy (FTIR), field emission scanning electron microscopy (FE-SEM), X-ray photoelectron spectroscopy (XPS), N_2 adsorption/desorption, ultraviolet–visible (UV–Vis) diffuse reflectance spectroscopy, and Zeta potential. XRD patterns, Rietveld refinement, and XPS spectra confirmed the formation of α-Ag_2WO_4, SBA-15, and α-Ag_2WO_4/SBA-15. XPS spectra evidenced the formation of metallic silver during analysis. FE-SEM images illustrated the deposition of α-Ag_2WO_4 nanocrystals mainly on the external surface of SBA-15. N_2 adsorption data showed that the textural properties of α-Ag_2WO_4/SBA-15 were similar to pure SBA-15. Zeta potential data demonstrated that all samples synthetized have negatively charged surface. The materials were tested as adsorbents for the dye cationic rhodamine B. The adsorption behavior of rhodamine B onto α-Ag_2WO_4, SBA-15, and α-Ag_2WO_4/SBA-15 correspond to Langmuir adsorption isotherm and pseudo-second-order kinetics. The maximum adsorption capacity of α-Ag_2WO_4/SBA-15 was up to 150 mg g^{-1} and 99% removal efficiency for RhB 20 mg L^{-1} in 15 min. Furthermore, 80% of RhB could be recuperated from adsorbents at pH 7.

Electronic supplementary material The online version of this article (doi:https://doi.org/10.1007/s10904-020-01560-3) contains supplementary material, which is available to authorized users.

✉ F. C. M. Silva
fmarquesilva@hotmail.com

L. K. R. Silva
larakribeiro@gmail.com

A. G. D. Santos
annegabriella@uern.br

V. P. S. Caldeira
viniciuscaldeira@uern.br

J. F. Cruz-Filho
joaoferreiradacruzfilho@gmail.com

L. S. Cavalcante
laeciosc@gmail.com

E. Longo
elson.liec@gmail.com

G. E. Luz Jr.
geraldoeduardo@gmail.com

[1] Department of Chemistry, Federal University of Piaui, Teresina, PI 64049-550, Brazil

[2] Department of Chemistry, FANAT State University of Rio Grande Do Norte, Mossoró, RN 59610-210, Brazil

[3] GERATEC-CCN-DQ, State University of Piaui, João Cabral S/N, Teresina, PI 64002-150, Brazil

[4] CDMF-Universidade Estadual Paulista, P.O. Box 355, Araraquara, SP 14801-907, Brazil

Graphic Abstract

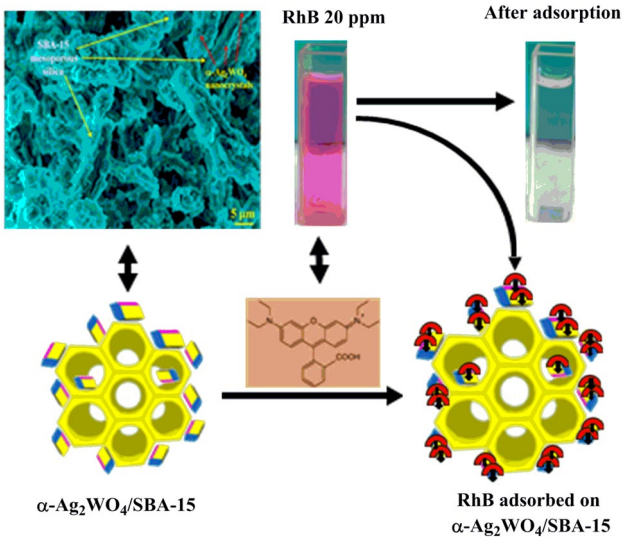

Keywords α-Ag_2WO_4 nanocrystals · Sonochemical · SBA-15 · Adsorption · Rhodamine

1 Introduction

Metallic tungstates are a family of inorganic materials represented by the general formula MWO_4 ($M = Ca^{2+}$, Sr^{2+}, Ba^{2+}, Fe^{2+}, Mn^{2+}, or Zn^{2+} and others) composed of covalent, ionic, and metallic ternary metal oxides. These compounds have received great attention because they are suitable for various technological applications, particularly as photocatalyst [1, 2]. Among tungstates, Ag_2WO_4 is outstanding due to its potential application in fields such as photocatalysis, semiconductors, antimicrobial, sensors, adsorbents, and bactericides [1–5]. Ag_2WO_4 exists as three types of polymorphic structure, the alpha (α) phase, which is thermodynamically stable, and metastable beta (β) and gamma (γ) phases that can easily transform into the α-phase [2, 4, 6]. α-Ag_2WO_4 has orthorhombic crystal structure with non-centrosymmetric space group ($Pn2n$) and (C_{2v}) point group symmetry formed by a complex three-dimensional structure. This structure includes distorted octahedral [WO_6] clusters and [AgO_n] clusters ($n = 7$, 6, 4 and 2), with polyhedrons such as: distorted deltahedral [AgO_6] clusters, distorted octahedral [AgO_6] clusters, distorted tetrahedral [AgO_4] clusters, and angular (AgO_2) bipyramids. These clusters form the unit cell with network parameters $a = 10.820$ Å, $b = 12.018$ Å; and $c = 5.900$ Å [1, 3, 7].

Silver tungstate can be synthesized by various methods, such as conventional hydrothermal, solid-state reaction, hydrothermal microwave assisted, coprecipitation, and sonochemical [1, 8–14]. The last method has shown promise because it is more rapid than conventional methods and promotes the homogeneous growth of the crystals, guaranteeing a material with reasonable purity, high crystallinity, and good optical properties [4, 10–13].

Recently, researchers deposited semiconductor (Ag_2WO_4) on a g-C_3N_4 support to improve silver tungstate activity in photocatalysis [15–17]. However, this support has limitations due to low specific area (~ 37 $m^2\ g^{-1}$). Ordered mesoporous materials [18], such as carbon nanotubes [19], carbon nanofibers [20], raw red clay [21], fibrous silica [22], zeolites ZSM-5 [22], and especially SBA-15 mesoporous silica [23–29], have aroused interest in the scientific community. Investigations have included insertion of metals and/or metal oxides [30], such as TiO_2 [28, 29, 31], Ti [32], CuO [33], Al [28], and WO_3 [27], into mesoporous support and formation of composite [34] for photocatalysis applications [18–22, 31, 35–40], adsorption [26], sensors [29, 41, 42], energy production [19, 20, 27, 43], electronic applications [44–46] etc.

In the context of support, SBA-15 (Santa Barbara Amorphous) stands out, because it has a defined pore structure with hexagonally arranged cylindrical and unidirectional mesopores (interconnected or not by secondary mesoporosity and/or microporosity in the silica walls). This structure gives the material properties, such as specific area (~ 1000 $m^2\ g^{-1}$), pore volume (up to 2.5 $cm^3\ g^{-1}$), average pore diameter between 2 and 10 nm, and thick silica wall responsible for good thermal and hydrothermal stability [47–51]. SBA-15 has application in catalysis and adsorption, but in the pure form, it presents low catalytic activity [50–53]. The dispersion of active sites (metals or metal oxides) on the

surface or on mesopores of SBA-15 is import, generating new mesostructured materials similar to pure SBA-15 and with greater application potential [50–55].

In applications for new materials, adsorption has received attention globally, owing to its use in removal of pollutants from aqueous solutions, its high efficiency, lower operating cost, and simple operation process [56, 57]. A good adsorbent needs high adsorption capacity and capability to rapidly establish adsorption equilibrium. Among the various pollutants discarded in the environment, rhodamine B is prominent because it is used in the textile, plastic, leather, and graphics industries [57, 58]. A concern with rhodamine in water is its carcinogenic effect, irritancy to the skin and eyes, and loss of 10 to 50% of dyes into wastewater during dyeing operation [50–61]. Dyes cause an aesthetically unpleasant effect on water, less than 1 ppm of some dyes discolor water, and may harm biological organisms and ecosystems [62, 63]. Thus, it is necessary to eliminate RhB from industrial wastewater before discharge into waterways [57].

Therefore, our paper investigated the synthesis of α-Ag_2WO_4 nanocrystals using the sonochemical method and deposition of α-Ag_2WO_4 nanocrystals on a mesoporous support of the SBA-15 type, by in situ sonochemical impregnation method, to obtain a new material α-Ag_2WO_4/SBA-15 and then evaluated its adsorption capacity for rhodamine B dye.

2 Materials and Methods

2.1 Materials

Silver nitrate ($AgNO_3$) (99% purity, Sigma-Aldrich); sodium tungstate dehydrate ($Na_2WO_4.2H_2O$) (99% purity, Sigma-Aldrich); citric acid ($C_6H_8O_7$) (99.5% purity, Sigma-Aldrich); tetraethyl orthosilicate (TEOS; $Si(OC_2H_5)_4$ (98% purity, Sigma-Aldrich); Pluronic P123 triblock copolymer ($EO_{20}PO_{70}EO_{20}$); hydrochloric acid (HCl) (37% purity, VETEC); and ethyl alcohol (C_2H_5OH) (95% purity, DINÂMICA) were employed in various synthesis methods.

2.2 Synthesis of α-Ag_2WO_4 Nanocrystals

α-Ag_2WO_4 nanocrystals were prepared by the sonochemical method as follows: 1×10^{-3} mol of $Na_2WO_4.2H_2O$ and 2×10^{-3} mol of $AgNO_3$ were dissolved separately in two beakers in 100 mL of deionized (DI) water. Then 4.2×10^{-5} mol of previously dissolved citric acid ($C_6H_8O_7$) was added to the $AgNO_3$ solution. The $AgNO_3$ solution was added to the Na_2WO_4 solution, and the mixture was ultrasonicated for 3 h in a Brason (model CPX-1800H) ultrasonic cleaner with a frequency of 42 Hz. After sonication, the precipitate was washed several times (~ 15) with deionized water and dried in a furnace at 65 °C for 10 h.

2.3 Synthesis of Pure Silica SBA-15

SBA-15 molecular sieve was prepared following the hydrothermal method used by Zhao et al. [18], in which TEOS, Pluronic P123, HCl, and DI water were reacted in the molar ratio 1.00:0.015:2.750:166.0. The mass of reagents was adjusted to prepare 100 g of gel based on this molar ratio. Procedure: P123 and HCl were added to DI water and the mixture was magnetically stirred for 2 h at 40 °C. Thereafter, TEOS was added and the mixture was magnetically stirred for 24 h at 40 °C. The gel obtained was transferred into a Teflon flask, which was placed in a stainless-steel autoclave and left to stand for 48 h at 100 °C. The yield obtained was cooled, filtered, washed with C_2H_5OH, dried at room temperature, and calcined at 500 °C for 5 h under synthetic air flow (100 mL min^{-1}).

2.4 Synthesis of α-Ag_2WO_4/SBA-15 by the In Situ Sonochemical Method

For α-Ag2WO4/SBA-15 synthesis, 0.300 g of SBA-15 molecular sieve was poured into 40 mL of DI water and sonicated for 30 min in a Brason (model CPX-1800H) ultrasonic cleaner with a frequency of 42 Hz. Meanwhile 1×10^{-3} mol of $Na_2WO_4.2H_2O$ and 2×10^{-3} mol of $AgNO_3$ were dissolved separately in beakers with 80 mL of deionized water. Then 4.2×10^{-5} mol of previously dissolved $C_6H_8O_7$ was added to the $AgNO_3$ solution. The Na_2WO_4 and $AgNO_3$ solutions were added to SBA-15 molecular sieve, and the mixture was ultrasonicated for 3 h in a Brason (model CPX-1800H) ultrasonic cleaner with a frequency of 42 Hz. After sonication, the precipitate was washed several times (~ 15) with DI water and dried in the furnace at 65 °C for 10 h.

2.5 Characterization of Adsorbents

Powder X-ray diffraction (XRD) patterns were measured using a diffractometer Rigaku Mini-Flex II model with Cu-Kα (λ = 0.15406 nm) as a radiation source, a nickel filter and applying an acceleration voltage and current of 40 kV and 30 mA. Bragg diffraction angles (2θ) were obtained in the ranges 0.5–10° (small angle) and 10–110° (wide angle) in 0.02° steps scanned at 1° min^{-1} for 1 s. The wide-angle XRD patterns were refined by the Rietveld method, Toolbar FullProf Suite Program©Software, version (3.00) using as input the crystallographic data of the crystallographic information file (CIF) Extension File No. 248969 [64] obtained from the ICSD (Inorganic Crystal Structure Database) website. The refinement was monitored by checking the correlation parameters *R*: expected *R*-factor (R_{exp}); weighted

profile *R*-factor (R_{wp}); chi square (χ^2); and goodness of fit (*S*). Fourier transform infrared spectra (FT-IR) (IRPrestige-21, Shimadzu) were obtained from 400 to 4000 cm^{-1}, with resolution 4 cm^{-1} and 40 scans. Samples were diluted to 1% in KBr solid (0.100 g KBr and 0.001 g sample) and then pressed (8 tons) to obtain the pellets to be analyzed. Raman spectra (Bruker SENTERRA with an Olympus BX50 microscope) were obtained with an automatic resolution of 3 cm^{-1} from 100 to 1200 cm^{-1} using 532 nm laser with output power 5 mW. UV–Vis spectroscopy of the solids were performed on the Shimadzu spectrophotometer, model UV-2600, in the region of wavelength from 200 to 800 cm^{-1}. Calculation of the optical band gap (E_g) values for our solids were performed using the relative reflectance data transformed for absorbance by the Kubelka–Munk method [65]. Scanning electron microscopy (SEM) was performed with a field emission electron microscope (FE-SEM, FEI, Quanta FEG 250). The textural properties of SBA-15, α-Ag_2WO_4 nanocrystals, and α-Ag_2WO_4/SBA-15 were obtained by Brunauer-Emmett–Teller (BET) and Barrett, Joyner and Halenda (BJH) methods. The measurements were made by nitrogen (N_2) adsorption–desorption at 77 K (ASAP 20210Micromeritics). The mesoporous parameter (a_0) value was obtained using the interplanar distances (*d*) associated with the (100) plane of the small angle diffractogram and then the wall thickness (w) was determined. For Zeta potential (Horiba Nanoparticle analyzer SZ-100) analysis, samples were diluted in DI water (2 mg sample to 50 mL water, pH ~ 6) and sonicated in a Brason (model CPX-1800H) ultrasonic cleaner with a frequency of 42 Hz for 30 min. Aliquots were introduced into the cuvette of the instrument and measurements were made in triplicate. X-ray photoelectron spectroscopy (XPS) (Thermo Fischer Scientific, model K-alpha) were obtained with Mg-Kα (1253.6 eV) monochromatic radiation. The binding energy was referenced to the C-1 *s* peak of surface carbon at 284.8 eV.

2.6 Adsorption Experiments

The adsorption measurements were conducted similar to the work of Dutta et al. [4], mixing 7 mg (0.0070 g) of adsorbents (α-Ag_2WO_4, α-Ag_2WO_4/SBA-15, and SBA-15) with 50 mL of RhB aqueous solutions. The mixture was placed in a catalytic cell under stirring (200 rpm at 298.15 K) coupled to a thermostatic bath until equilibrium is attained. The effect of pH, contact time, initial RhB concentration, solution temperature, and dosage were studied. The pH range of RhB solution was adjusted by HCl or NaOH (0.5 mol L^{-1}). To study of time, the experiments were done for 5, 10, 20, 40, and 60 min. In the study of effect of RhB concentration, the time was fixed at 15 min and initial RhB concentrations (2.5, 5, 10, 15, 20, 30, 40, and 50 mg L^{-1}) for α-Ag_2WO_4, α-Ag_2WO_4/SBA-15; 60 min and initial RhB concentrations (2.5, 5, 10, 15, and 20 mg L^{-1}) for SBA-15. To study pH, the mixture of 7 mg of adsorbents with 50 mL of RhB 20 mg L^{-1} was conducted varying the pH (1, 3, 3.5, 5, 7, and 9). The effects of temperature was studied using a mixture of 7 mg of adsorbents with RhB (40 mg L^{-1} of α-Ag_2WO_4 or α-Ag_2WO_4/SBA-15 and 20 mg L^{-1} of SBA-15) at the temperatures of 298.15, 308.15, and 318.15 K. In the study of dosage, 50 mL de RhB 50 mg L^{-1} was mixed with dosage of 0.140, 0.176, 0.352, and 0.700 g L^{-1} of α-Ag_2WO_4 or α-Ag_2WO_4/SBA-15 in pH 3.5 and for 30 min. At the end of adsorption experiments, the dye concentration was determined by measuring the characteristic absorbance of RhB, $\lambda_{max} = 554$ nm [66], and comparing with a calibration curve. All adsorption experiments were conducted in triplicate, and the average value was taken. The aqueous RhB solutions were prepared using DI water. The adsorption capacity of the adsorbent for RhB was calculated through the following equation:

$$q_e = \frac{(C_0 - C_e)}{W} \times V \tag{1}$$

where C_0 is the initial concentration of dye in solution (mg L^{-1}), C_e (mg L^{-1}) is the equilibrium concentrations of RhB, V is the volume in L, and W is the weight of adsorbent (g).

The performance of adsorbents is measured in terms of removal efficiency (Re%) defined as:

$$\mathrm{Re} = \frac{(c_0 - c_e)}{c_e} \times 100 \tag{2}$$

In this study, three classical adsorption models Langmuir (Eqs. 3 and 4), Freundlich (Eq. 5), and Temkin (Eq. 6) isotherms were used to fit the RhB experimental equilibrium adsorption data [57, 67–71]:

$$\frac{C_e}{q_e} = \frac{C_e}{q_m} + \frac{1}{q_m K} \tag{3}$$

$$R_L = \frac{1}{1 + Kc_e} \tag{4}$$

$$\log q_e = \frac{1}{n} \log c_e + \log K_f \tag{5}$$

$$q_e = \frac{1}{n_T} \ln c_e + \frac{1}{n_T} \ln K_T \tag{6}$$

where q_e (mg g^{-1}) is the capacity of adsorption; K (L mg^{-1}) the Langmuir isotherm constant that relates to the affinity of binding sites and describes the intensity of the adsorption process; Q_m (mg g^{-1}) is the theoretical maximum adsorption capacity; R_L is a dimensionless separation factor, K_f (mg g^{-1}) and n are Freundlich isotherm constants;

K_T is a constant that encompasses the equilibrium constant; n_T indicates the reactivity of the material's energy sites [71–74]. For the kinetic study, a mixture of 7 mg of adsorbent (α-Ag_2WO_4, α-Ag_2WO_4/SBA-15, or SBA-15) with 50 mL RhB (20 mg L^{-1}) was reacted for specified times. The kinetic study was adjusted to the pseudo-first order and pseudo-second order model represented by the following relation [56, 71, 75, 76]:

$$\ln\left(q_e - q_t\right) = \ln q_e - K_t t \tag{7}$$

$$\frac{t}{q_t} = \frac{1}{k_2 q_e^2} + \frac{t}{q_t} \tag{8}$$

$$h = k_2 q_e^2 \tag{9}$$

where q_e (mg g^{-1}) is adsorption capacity; q_t (mg g^{-1}) is adsorption capacity time t); K_1 and K_2 are the rate constant of first-order and second-order adsorption respectively.

The thermodynamic parameters ΔG° (Gibbs free energy), ΔH° (enthalpy), and ΔS° (entropy) were obtained as following:

$$\Delta G^\circ = -RT \ln K \tag{10}$$

$$K = \frac{q_e}{c_e} \tag{11}$$

$$\Delta G^\circ = \Delta H^\circ - T\Delta S^\circ \tag{12}$$

where R is the gas constant (J mol^{-1} K^{-1}), T is the absolute temperature and K is the equilibrium constant at temperature T. The values of ΔH° and ΔS° were obtained by plotting the graph of ln K as a function of T^{-1}, obtaining a line with the equation of angular and linear coefficient equal to ΔH°/R and ΔS°/R, respectively [71, 73, 77]. Desorption of RhB (20 mg L^{-1}) adsorbed on the absorbents was performed by changing the pH. Adjusting the pH of the solution after desorption (pH 7, 10 and 12) promoted the instant desorption of RhB from adsorbents.

3 Results and Discussion

3.1 X-Ray Diffraction (XRD)

Both samples exhibit three characteristic XRD peaks (Fig. 1a), which are indexed in (100), (110), and (200) planes and assign the pore and mesopore structure of the two-dimensional hexagonal structure with (*P6mm)* space group related to SBA-15 molecular sieve [16, 47, 55]. The presence of these XRD peaks, with intensity similar to pure SBA-15 matrix, in the supported tungstate sample α-Ag_2WO_4/SBA-15, indicates preservation of the mesoporous organization of SBA-15 and that the mesoporous structure was not destroyed [78]. The peaks of α-Ag_2WO_4/SBA-15 shifted to the left (lower values of 2θ) relative to pure SBA-15, as shown in Fig. 1a, which may be related to large mesopores and increased hexagonal parameter [49, 79], as will be discussed in relation to the textural properties. Such shift can be assigned to the substitution of the shorter Si–O bond for longer Ag–O bond, phenomenon similar to what occurred in LaSBA-15 as reported by Bendahou et al. [80]. A widening

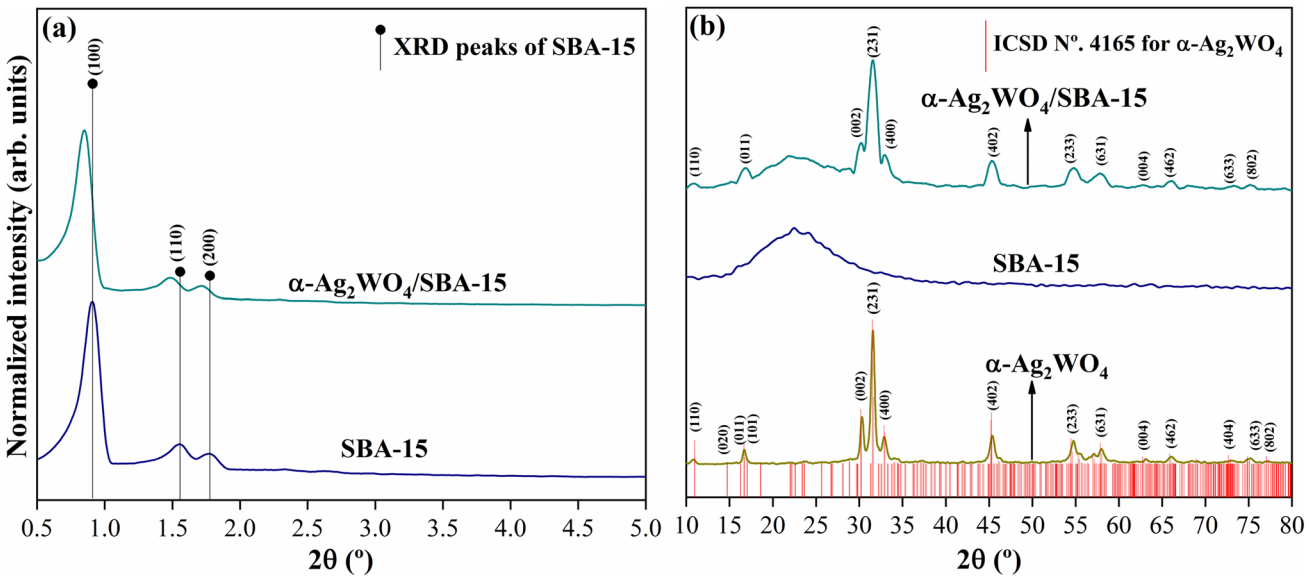

Fig. 1 **a** Small angle X-Ray diffraction patterns of SBA-15 molecular sieve and α-Ag_2WO_4/SBA-15 nanocomposite, **b** Wide-angle X-ray diffraction patterns of α-Ag_2WO_4 nanocrystals, SBA-15 molecular sieve and α-Ag_2WO_4/SBA-15 nanocomposite

of the peaks in the nanocomposite α-Ag_2WO_4/SBA-15 indicates reduction in crystal size owing to the deagglomeration of α-Ag_2WO_4 crystals on the external surface of SBA-15, promoted by the in-situ sonochemical method. The small-angle XRD patterns of SBA-15 and α-Ag_2WO_4/SBA-15 are similar, indicating that the in-situ sonochemical impregnation method favored the SBA-15 molecular sieve for the structure of α-Ag_2WO_4/SBA-15. Figure 1b shows the presence of XRD peaks, which are consistent with α-Ag_2WO_4 crystals with orthorhombic structure, with (*Pn2n*) space group and (C_{2v}) symmetry group [6, 7], in accordance with the inorganic crystal structure database (ICSD Card No. 4165) [81]. This indicates that the α-phase of Ag_2WO_4 crystals remained clean. The intensity of the XRD peaks are indicative of high periodicity of lattice, structural order at long-range, and reasonable crystallinity [4, 12]. The intense and broad XRD peak located at around $2\theta \cong 22.6°$ is characteristic of amorphous silica (SiO_2) [55, 82]. The diffractograms at low and wide angles are coherent and show retention of α-Ag_2WO_4 in a single phase, and formation of α-Ag_2WO_4/SBA-15, without altering the silver tungstate phase and preserving the structure of the SBA-15 molecular sieve. No conclusions could be drawn about the presence of metallic silver (Ag^0) nanoparticles in the lattice of α-Ag_2WO_4 crystals from XRD measurements [83]. All diffraction peaks are in good agreement with the respective Inorganic Crystal Structure Data (ICSD) Base No. 4165 and the recent literature [84].

3.2 Rietveld Refinement of XRD Patterns

The structural refinement (Fig. 2a) obtained by the Rietveld method is consistent with the single crystalline phase with orthorhombic structure for α-Ag_2WO_4 nanocrystals and excellent agreement with their respective ICSD No. 4165, validated by indexing all peaks [10]. The widening of the $Y_{Obs} - Y_{Calc}$ line of the nanocomposite α-Ag_2WO_4/SBA-15 (Fig. 2b) is due to pure amorphous SBA-15. The quality indices and relative crystallinity of Rietveld Refinement are shown in Table 1.

The values of the parameters R_p, R_{wp}, R_{exp}, and χ^2 for Ag_2WO_4 are consistent with a single crystalline phase with

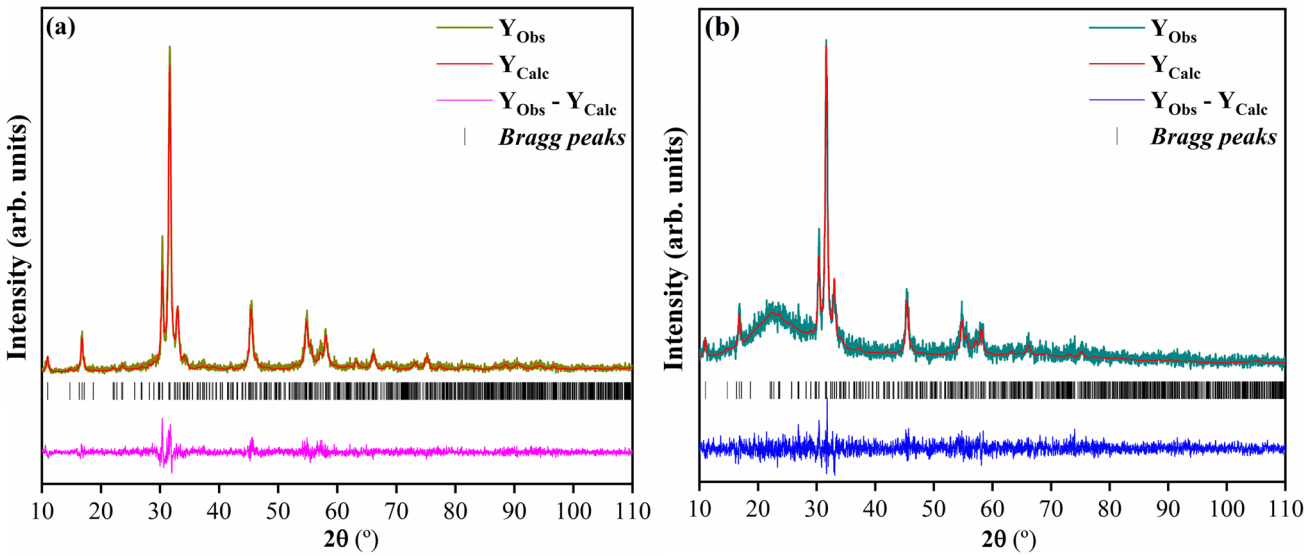

Fig. 2 Rietveld Refinement of XRD patterns: **a** α-Ag_2WO_4 nanocrystals and **b** α-Ag_2WO_4/SBA-15 nanocomposite

Table 1 Rietveld refinement for α-Ag_2WO_4 and α-Ag_2WO_4/SBA-15 samples

Samples	Quality indices					*R.C (%)
	*R_p	*R_{wp}	*R_{exp}	*χ^2	S	
α-Ag_2WO_4	12.9	16.3	12.8	1.6	1.2	100
α-Ag_2WO_4/SBA-15	17.1	24.0	19.8	1.6	1.3	20

*R_p (profile factor), *R_{wp} (weighted profile factor), *R_{exp} (expected weighted profile R- factor),*χ^2 (adjustment factor) and S (goodness of fit). The values of R_p, R_{wp}, and R_{exp} are given in %. Relative crystallinity (R.C. %) $= \frac{I_{obs} - I_{background}}{I_{obs}} x100$, I_{obs} is the total integrated area and $I_{background}$ is the integrated area of the amorphous region baseline

the orthorhombic structure for α-Ag_2WO_4 already reported in the literature [6, 10]. The values of R_p, R_{wp}, and R_{exp} for mesoporous nanocomposite α-Ag_2WO_4/SBA-15 are higher than α-Ag_2WO_4, which must be related to the influence of silica in pure amorphous SBA-15. However, this does not compromise the refinement [10, 85]. Considering χ^2 (1.6 for both α-Ag_2WO_4 and α-Ag_2WO_4/SBA-15), S (> 2), and the difference between the $Y_{Obs\ -}\ Y_{Calc}$ line (background), this refinement is of acceptable quality. The parameters χ^2 (1.6 to both) and S (> 2) agree with the literature [6].

The Rietveld refinement data was also employed to calculate the relative crystallinity (%) in the α-Ag_2WO_4nanocrystals/SBA-15 samples. In this composite, the relative crystallinity (%) is equal to the weight percentage of α-Ag_2WO_4 (crystalline solid) because the SBA-15 support is amorphous. Therefore, a relative crystallinity of 20% in composite mesoporous α-Ag_2WO_4/SBA-15 means that the nanocomposite contains about 20% α-Ag_2WO_4.

3.3 Raman Spectra

M-Raman spectroscopy provides information on the degree of structural order or disorder in the lattice of α-Ag_2WO_4 nanocrystals deposited on the SBA-15 support. The MR spectrum for α-Ag_2WO_4 nanocrystals (Fig. 3a) revealed only the presence of 5 Raman-active vibrational modes. The other Raman modes (B_{1g}, A_{2g}, and B_{2g}) were not detectable experimentally due to their low intensities and the small size of the α-Ag_2WO_4 nanocrystals. The more intense Raman-active vibrational modes relate to the symmetric stretching of (←O←W→O→) bonds of the octahedral

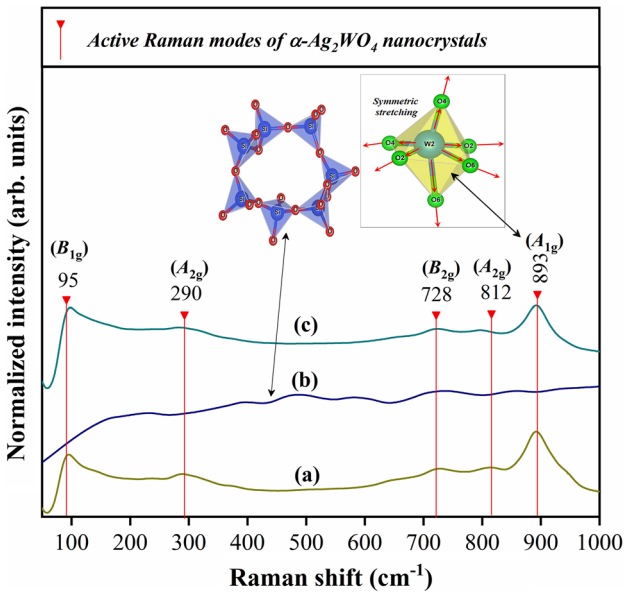

Fig. 3 Raman spectra: a α-Ag_2WO_4 nanocrystals, b SBA-15 molecular sieve, and c α-Ag_2WO_4/SBA-15 nanocomposite

[WO_6] clusters (see inset Fig. 3a) rather than to the external vibrational modes of the distorted [AgO_z] clusters (z = 7, 6, 4, and 2) and the other bending modes of the Ag–O–W units [8, 86]. The active modes observed around 300 cm^{-1} correspond to distorted [AgO_z] clusters (z = 7, 6, 4 and 2) [8] and/or torsional motion of distorted [WO_6] clusters. The Raman-active vibrational modes at 95, 290, 728, 812, and 893 cm^{-1} are displaced compared to those reported in the literature [8, 86]. This can be associated with several factors, such as the synthesis method, crystal mean size, interaction force between ions, and structural order in the lattice [86]. In Fig. 3b, the M-Raman spectra for SBA-15 molecular sieve exhibit Raman-active vibrations with lower intensities, which are assigned to O–Si–O symmetric vibrational modes, arising from isolated four-membered rings of tetrahedral [SiO_4] clusters and breathing vibrations of three-membered rings of tetrahedral [SiO_4] clusters (see inset Fig. 3b) [87, 88]. α-Ag_2WO_4/SBA–15 (Fig. 3c) also present 5 active vibration modes identified as B_{1g}, A_{2g}, B_{2g}, A_{2g}, B_{2g}, and A_{1g} [8, 86]. The peaks, which are related to the vibration modes of the α-Ag_2WO_4/SBA-15 sample, are less intense than those of the α-Ag_2WO_4 sample because of the dilution effect of SBA-15. The peaks are also displaced relative to those of α-Ag_2WO_4, implying interaction of α-Ag_2WO_4 with the SBA-15 support [55], which is consistent with the XRD analysis. The absence of other modes of vibration can be attributed to low peak intensity and indicates a greater degree of short-range disorder in the solids [8, 88].

3.4 FT-IR Analysis

According to the literature [17, 88, 89], IR spectrum provides information on the degree of structural order–disorder of the metal–oxygen bonds present in coordination clusters in an orthorhombic lattice. In Fig. 4a, the FT-IR spectra for α-Ag_2WO_4 nanocrystals exhibit only two IR-active vibrational modes, which are ascribed to one $1A_u$ mode at around 837 cm^{-1} and one $1A_u$ mode at approximately 889 cm^{-1}. These two A_u modes are attributed to the asymmetric stretching vibrations of the (→O→W→O→)/(←O←W←O←) bonds within the distorted octahedral [WO_6] clusters (see the inset in Fig. 4a). A strong absorption band in 3400 cm^{-1} and weak peak in 1650 are assigned the vibration of –OH, which indicated water molecules on α-Ag_2WO_4 surface [17]. The intensity of such band in the α-Ag_2WO_4 is greater than in the SBA-15, which can be attributed to fact that α-Ag_2WO_4 was dried only at 65 °C, while SBA-15 was calcined at 550 °C, and before analysis samples were not heated to remove adsorbed water. The FT-IR spectrum (Fig. 4c) showed some significant changes in relation to IR spectrum of pure SBA-15 molecular sieve (Fig. 4b). The spectral region from 400 cm^{-1} to 2000 cm^{-1} revealed the presence of five IR-active vibration modes. The

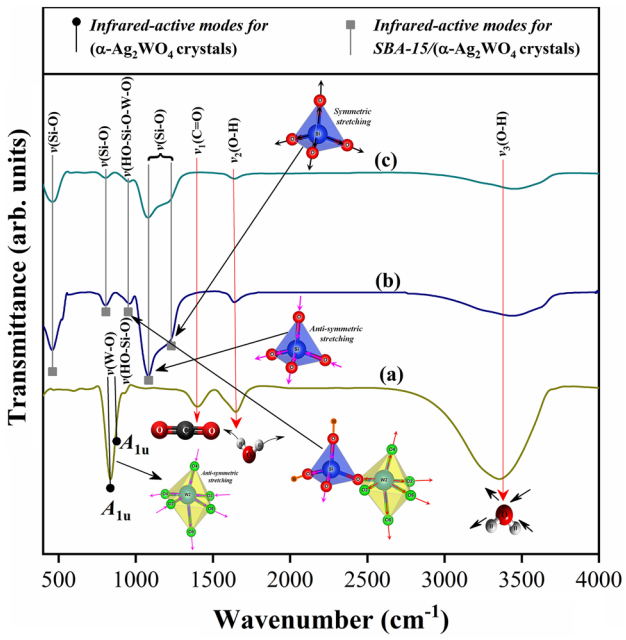

Fig. 4 FTIR spectra: a α-Ag_2WO_4 nanocrystals, b SBA-15 molecular sieve, and c α-Ag_2WO_4/SBA-15 nanocomposite

first IR-active vibrational mode at around 461 cm^{-1} is related to the ν(O–Si–O) bonds of tetrahedral [SiO_4] clusters. The second vibrational mode at close to 805 cm^{-1} and fourth very intense at about 1082 cm^{-1} and attributed to anti-symmetric stretching vibrations of ν(O–Si–O) bonds present in the tetrahedral [SiO_4]. The third IR-active vibrational mode near 960 cm^{-1} is related to the symmetric stretching vibrations of ν_{sym}(O–Si–O–H) bonds in silanol groups [16, 54]. Moreover, this IR band is displaced to low wavenumber at around 957 cm^{-1} and is typical of ν(HO–Si–O–W–O) bonds affected by interaction of distorted octahedral [WO_6] clusters with tetrahedral [SiO_4] clusters [54, 55, 90, 91]. The fifth IR-active vibrational mode is a shoulder at 1213 cm^{-1}, corresponding to anti-symmetric stretching vibrations of ν(O–Si–O) bonds.

3.5 Morphologies

The literature reports the basal morphology of rods for α-Ag_2WO_4 nanocrystals [1, 8, 12], but Fig. 5a illustrated the presence of several agglomerated nanocrystals with no defined morphology, which could be attributed to the

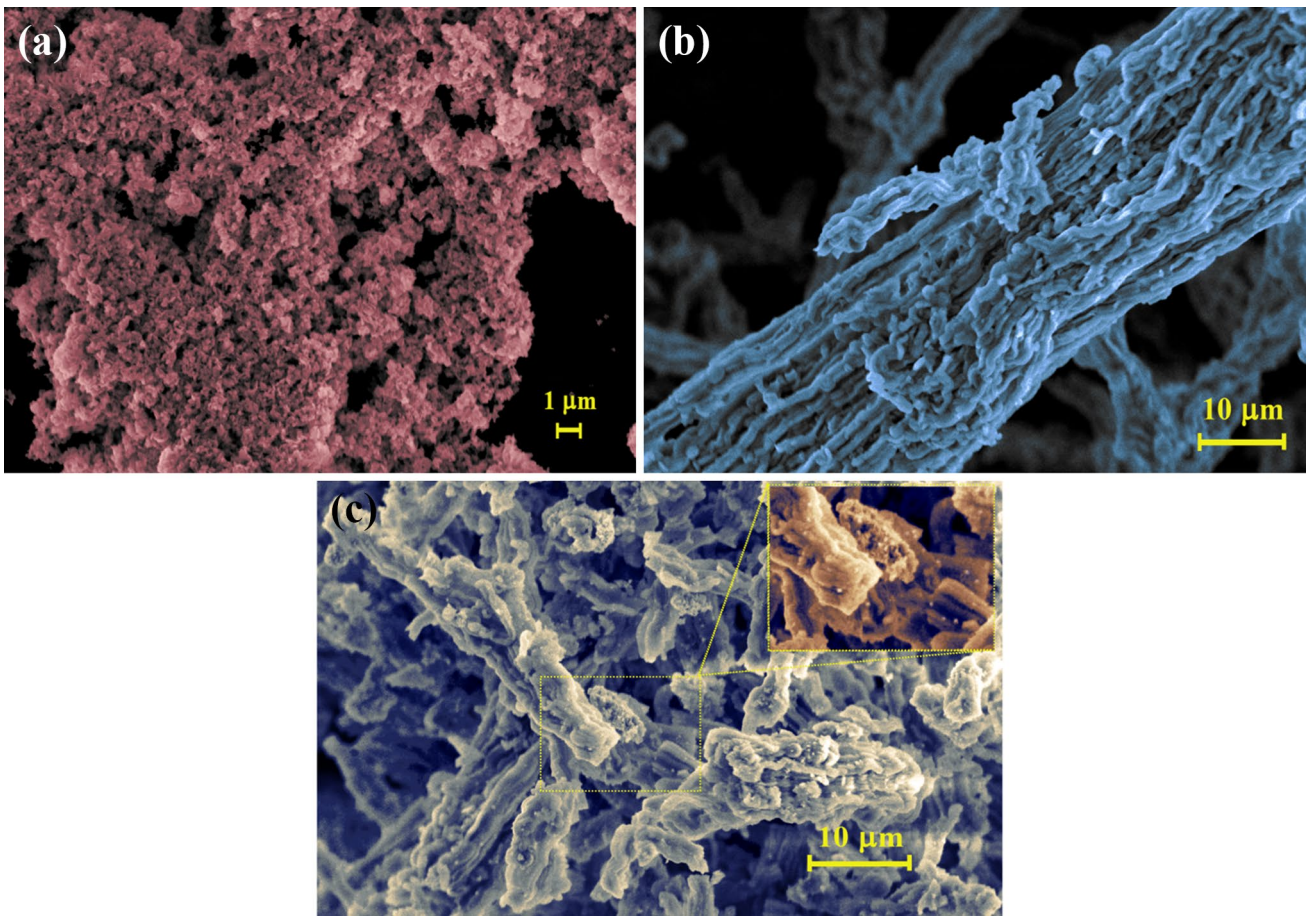

Fig. 5 FE-SEM images for **a** α-Ag_2WO_4 nanocrystals, **b** SBA-15 molecular sieve, and **c** α-Ag_2WO_4/SBA-15 nanocomposite

influence of citric acid as chelating agent in the formation of α-Ag_2WO_4 nanocrystals. The pure SBA-15 matrix (Fig. 5b) exhibits irregular elongated tube-like shapes with different diameters and lengths. Moreover, there are some interconnections between these tubes, which can be related to growth mechanism by means of self-assembly. This structure is characteristic of this molecular sieve, i.e. fibrous morphology with cylindrical tubes [55]. The micrograph (Fig. 5c) of α-Ag_2WO_4/SBA-15 illustrates that the structure of SBA-15 was maintained and that the α-Ag_2WO_4 nanocrystals are deposited mainly on the external surface of the support (SBA-15). This result is consistent with the XRD results and adsorption and desorption of N_2. Figure 5c shows agglomerated α-Ag_2WO_4 nanocrystals, which is consistent with larger reductions in textural properties by the in-situ sonochemical impregnation method, since the agglomerates of particles on the external surface may further block the pores of SBA-15.

3.6 N_2 Adsorption–Desorption Studies

Figure 6a present the BET with N_2 isotherm for α-Ag_2WO_4 nanocrystals. According to IUPAC classification, this is a type III isotherm related to nonporous or macroporous materials [92]. α-Ag_2WO_4/SBA-15 and SBA-15 exhibit peculiar type IV(a) isotherms of mesoporous materials [54, 55]. The hysteresis of α-Ag_2WO_4/SBA-15 and SBA-15 is type H1, characterizing the existence of mesoporous materials with uniform and parallel cylindrical pores of open ends [54, 55, 93]. The very parallel hysteresis loop in the P/P_0 region between 0.6 and 0.8 shows the mesoporous structure of the materials and the uniform distribution of pore size, which indicates that the insertion of the inorganic material (α-Ag_2WO_4) did not destroy the structure of SBA-15, and is consistent with XRD results. Figure 6b shows that the average pore diameter of SBA-15 and α-Ag_2WO_4/SBA-15 was between 6.4 and 7.5 nm; their similar pore sizes suggest that α-Ag_2WO_4 impregnation did not change the SBA-15 mesoporous structure. The larger pore diameter of α-Ag_2WO_4/SBA-15 was expected with α-Ag_2WO_4 deposition within the pores and on the external surface. Deposition inside the pores began by filling the primary mesoporous (smaller size) pores and then the secondary mesoporous (larger size) pores, causing an increase in the average diameter. α-Ag_2WO_4deposition within the mesopores is promising and positive as it generates active sites in the mesopores.

Table 2 shows the textured properties and zeta potential of α-Ag_2WO_4, SBA-15, and α-Ag_2WO_4/SBA-15. α-Ag_2WO_4 presented a surface area of 21.05 $m^2\ g^{-1}$. This is higher than generally reported for other silver-based materials (of the order 6 $m^2\ g^{-1}$) [13, 94], but lower than that of β-Ag_2WO_4 in nanospheres [4, 95], and similar to the 24 $m^2\ g^{-1}$ obtained for the Ag_3PO_4 analogue [93]. The observed value is consistent with the type of isotherm associated with nonporous or macroporous material as this material has interstitial pores with a diameter of 31.81 nm. The values of specific area (S_{BET} $m^2\ g^{-1}$), external areas ($S_{external}$), micropore area (S_{micro} $m^2\ g^{-1}$), pore volume (V_{pore} $cm^3\ g^{-1}$), and micropore volume (V_{micro} $cm^3\ g^{-1}$) of α-Ag_2WO_4/SBA-15 decrease compared to pure SBA-15. This is consistent with the dispersion of α-Ag_2WO_4 on the outer surface of SBA-15 causing blockage of the pore channels and with α-Ag_2WO_4 deposition within the pores [55]. Thus, SEM images showing the crystals of α-Ag_2WO_4/SBA-15 on the surface of SBA-15 and the observed textural and pore properties are all in

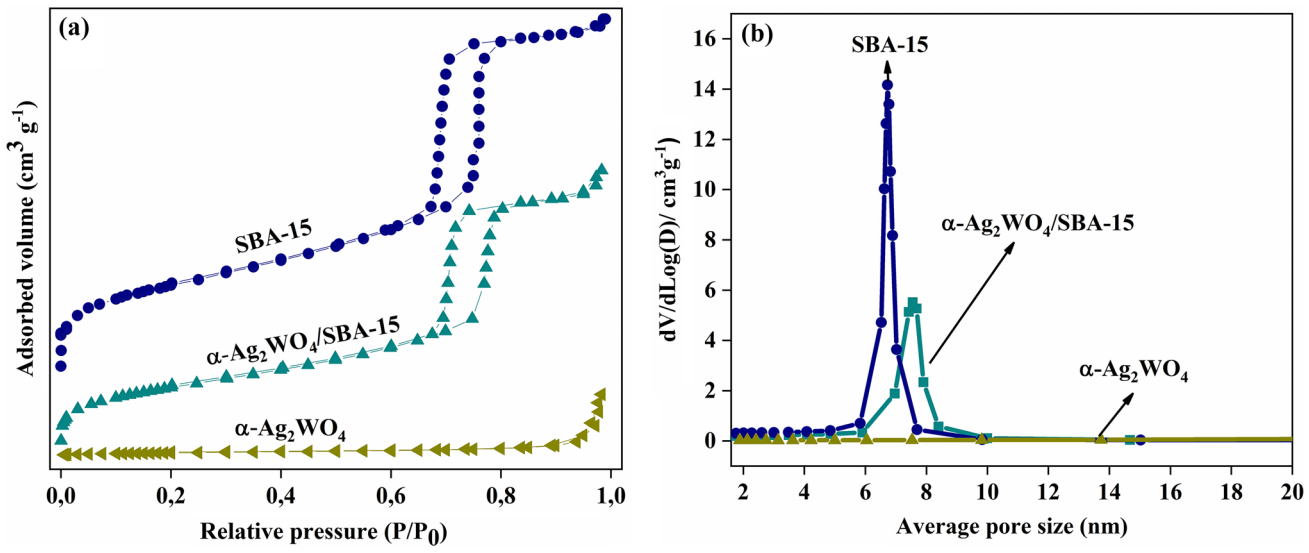

Fig. 6 **a** N_2 adsorption–desorption isotherms and **b** pore diameter distribution of α-Ag_2WO_4 nanocrystals, SBA-15 molecular sieve, and α-Ag_2WO_4/SBA-15 nanocomposite

Table 2 Textural Properties and zeta potential of α-Ag_2WO_4, SBA-15, and α-Ag_2WO_4/SBA-15 samples

Samples	*S_{BET} ($m^2\ g^{-1}$)	$S_{(external)}$ ($m^2\ g^{-1}$)	S_{micro} ($m^2\ g^{-1}$)	V_{poro} ($cm^3\ g^{-1}$)	V_{micro} ($cm^3\ g^{-1}$)	*Dp (nm)	*a_0 (nm)	*w (nm)	ζ (pH 6)
SBA-15	677.0	572.7	104.3	0,86	0.04	6.4	11.2	4.9	−63.3
α-Ag_2WO_4	21.0	22.9	15.4	0.12	–	31.81	–	–	−66.9
α-Ag_2WO_4/SBA-15	375.8	339.4	36.4	0.62	0.01	7.5	12.1	4.7	−51.4

[a]$a_0 = 2d(100)/\sqrt{3}$; *$w = a_0 - Dp$; *$S_{(BET)}$: Specific surface area obtained by using BET method Brunaer–Emmet–Teller); values extracted from BJH (Barret–Joyner–Halenda), desorption average pore diameter. ζ (Zeta potential measurements at pH ~ 6)

agreement. The increase in pore diameter in α-Ag_2WO_4/SBA-15 may in part be attributed to the effect of the interstitial pores of α-Ag_2WO_4 deposited on the surfaces and within the inner pores of SBA-15.

All the zeta potentials are negative (Table 2), which indicates that α-Ag_2WO_4, SBA-15, and α-Ag_2WO_4/SBA-15 particles are negatively charged. The negatively charged surface on α-Ag_2WO_4 is due to the presence of WO_4^{2-} groups, which are consistent with the preferential dissolution of Ag^+ [4, 94]. The potential value of α-Ag_2WO_4 (−66.93 mV) is lower than the −30 mV and −42.24 mV reported in the literature [4, 94]. This difference may be related to differences between the pH at which the measurements were obtained (pH ~ 6) and the absence of salts, which alter the ionic strength of the medium, in samples preparation. SBA-15 also exhibited negative potential; however, this value is not attributed to the negative charge of SBA-15, but to OH^- groups adsorbed on the surface of the SBA-15 or isolated silanol groups deprotonated [96, 97]. The zeta potential of α-Ag_2WO_4/SBA-15 is less negative than α-Ag_2WO_4 and SBA-15. This implies that α-Ag_2WO_4 on external surface of SBA-15 decreases the contribution of the OH^- groups to the SBA-15 surface potential, and that dissolution of Ag^+ to produce WO_4^{2-} groups on the SBA-15 surface may be less significant. The study of zeta potential of α-Ag_2WO_4 as a function of pH has already been reported in literature [4, 97], indicating that α-Ag_2WO_4 has negative zeta potential in a wide pH range (1–7) and an isoelectric point (pH_{iep}) equal to 0.6.

3.7 X-Ray Photoelectron Spectroscopy (XPS)

XPS spectra can provide information on chemical composition, oxidation state of the elements, and electronic states [98]. The XPS spectrum for α-Ag_2WO_4 nanocrystals (Fig. 7a) shows the presence of the elements Ag, W, and O. Moreover, as illustrated in inset Fig. 8a, the nanocrystals could have interacted with the X-Ray beam on the surface, which represented a manifestation of the chemical behavior of pristine α-Ag_2WO_4. The XPS spectrum of SBA-15 (Fig. 7b) shows the presence of elemental Si and O. The inset Fig. 7b illustrates the interaction of the photon beam with the SBA-15 surface. The XPS spectrum of α-Ag_2WO_4/SBA-15 is also displayed in Fig. 7c and inset and demonstrates the presence of the elements Ag, W, O, and Si. The carbon (C) that appears in all samples results from the internal standard used to calibrate the binding energy of the other elements [14]. The presence of very sharp XPS peaks referring to the Ag, W, O, and Si elements confirms the presence the high purity of the samples. Moreover, the presence of all the expected elements indicates the success of the synthesis method for α-Ag_2WO_4 nanocrystals supported on SBA-15 molecular sieve, as already indicated by the XRD patterns and Rietveld refinement data. Finally, the XPS spectrum of α-Ag_2WO_4/SBA-15 indicates that the most pronounced XPS peak is O-1 *s* with binding energy in the region from 530 to 542 eV; this intensity must be related to a high total oxygen concentration on the surface with the combined contributions from α-Ag_2WO_4 nanocrystals and SBA-15 (SiO_2).

XPS spectra at high resolution contains additional information. The Ag-3*d* peak in α-Ag_2WO_4 nanocrystals and α-Ag_2WO_4/SBA-15, and the O-1 *s* in α-Ag_2WO_4/SBA-15 peak are discussed in this section, aiming, respectively, to investigate the presence of metallic silver, which could be generated during analysis of XPS, and to find evidence of interactions between the α-Ag_2WO_4 nanocrystals and SBA-15. The Ag-3*d* doublet at 368 eV and 375 eV represents Ag-$3d_{5/2}$ and Ag-$3d_{3/2}$ attributed to Ag^+ [3, 99]. These binding energies are slightly displaced since they usually appear at 367 eV and 374 eV. This displacement is indicative of the presence of metallic silver (Ag^0) on crystal surface [96, 99]. Deconvolution of the Ag-3*d* XPS peaks for α-Ag_2WO_4 nanocrystals and α-Ag_2WO_4/SBA-15 presented four components, indicating that more than one valence state is present. As displayed in Fig. 8a, the α-Ag_2WO_4 nanocrystals exhibit two low intensity peaks at 367.5 and 373.6 eV, assigned to Ag^+ ions, and two high intensity peaks at 368.4 and 374.5 eV, assigned to the Ag^0 [100, 101]. The XPS spectrum of the α-Ag_2WO_4/SBA-15 (Fig. 8b) likewise has 4 peaks corresponding to Ag^+ and Ag^0. The area of Ag^0 peaks for α-Ag_2WO_4/SBA-15 nanoparticles is less than α-Ag_2WO_4. This suggests that SBA-15 silica support may reduce the formation of Ag^0 nanoparticles. The Ag-3*d* peaks shift to higher binding energy (BE) in the α-Ag_2WO_4 nanocrystals.

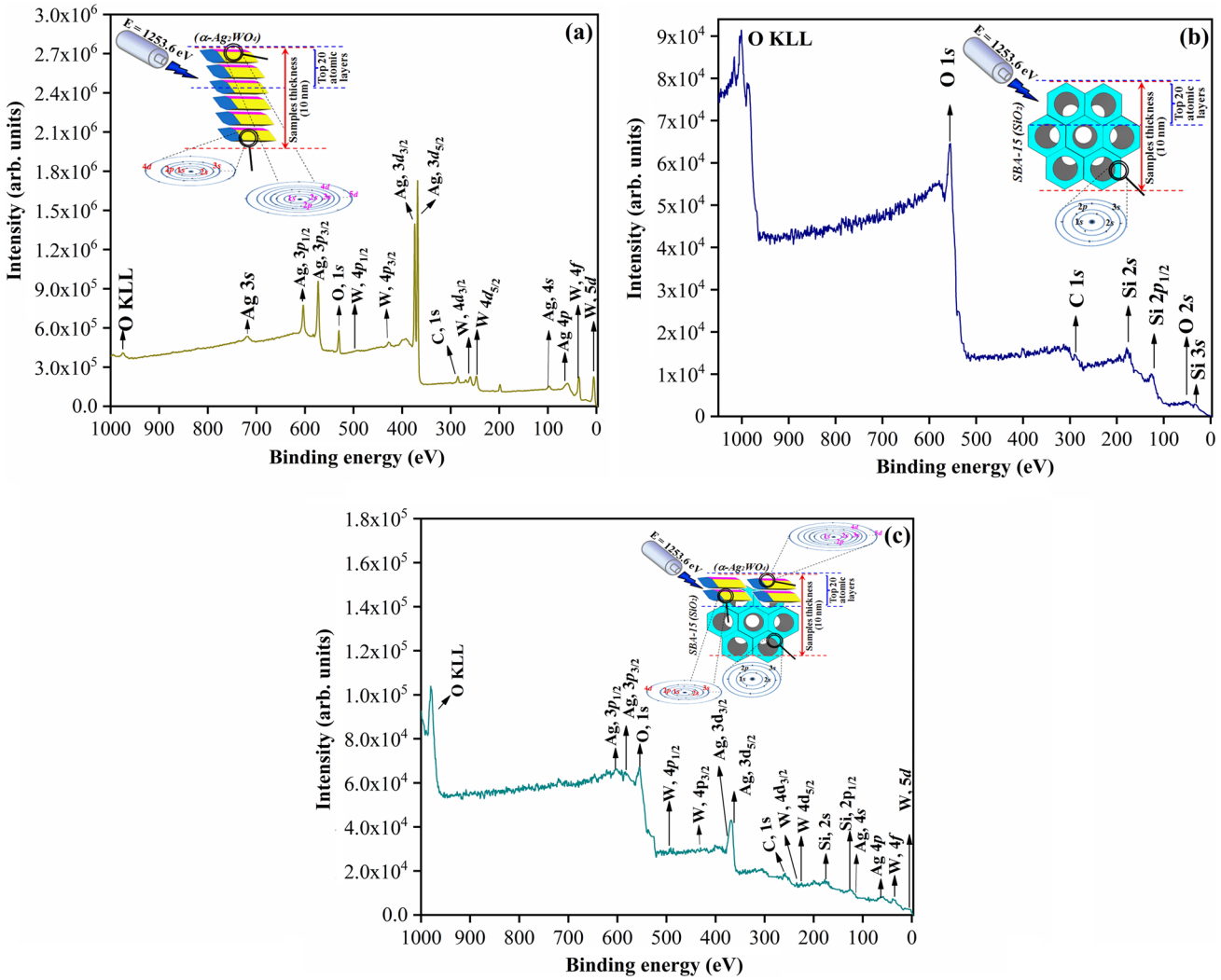

Fig. 7 XPS spectra: **a** α-Ag_2WO_4 nanocrystals, **b** SBA-15 molecular sieve, and **c** α-Ag_2WO_4/SBA-15 nanocomposite

This behavior is indicative of chemical interaction between the Ag and the SBA-15 support and indicates that the surface is negatively charged and that the surrounding silver species may also have an influence [102]. Therefore, the XPS data signifies an interaction between Ag and the SBA-15 support in the α-Ag_2WO_4/SBA-15 nanocomposite. This interaction may be related to an observed change in the degeneracy of 3*d* orbitals in α-Ag_2WO_4/SBA-15, the peak area of Ag-3$d_{5/2}$ is smaller than that of the Ag-3$d_{3/2}$.

Figures 8(c–e) demonstrate that the O-1 *s* peak at 525–545 eV can be deconvoluted into two (α-Ag_2WO_4, Fig. 8c), three (SBA-15, Fig. 8d), or four (α-Ag_2WO_4/SBA-15, Fig. 8e) components. The O-1 *s* peak of α-Ag_2WO_4 nanocrystals is a broad profile at 530 and 531 eV, suggesting different chemical bonds between the Ag and O, and the W and O [3, 15]. SBA-15 O-1 *s* peaks appear at ~ 533 and ~ 534 eV. The 533 eV peak is deconvoluted in two components corresponding to OH sites arising from water chemisorbed on the surface of SBA-15 [15]. The O-1 *s* peak at ~ 534 eV is ascribed to Si–O–Si bonds [103]. The O-1 *s* peak of α-Ag_2WO_4/SBA-15 splits into four components: O–H groups and/or water molecules chemisorbed on the surface of nanocrystal at ~ 533.5 eV [15]; Si–O–Si bonds at ~ 534 eV [103]; and O–Ag–O bonds or O–W–O bonds at ~ 531 eV [3]. These binding energy values are higher than previously reported [3, 15, 102, 103]. For O-1 *s*, higher binding energies signify less oxygen on the surface or more positive surfaces. However, the surface must still be negative since Ag-*d* electrons also show high binding energies. O has a high surface concentration in the nanocomposite; therefore, it must have experienced a more positive environment to shift to higher binding energy. This result should be related to the influence of the surrounding oxygen in various chemical interactions with Si, O, Ag, W, and H as well as and the influence of nano α-Ag_2WO_4 [102, 104]. When a neighborhood electron is removed, the effective charge felt

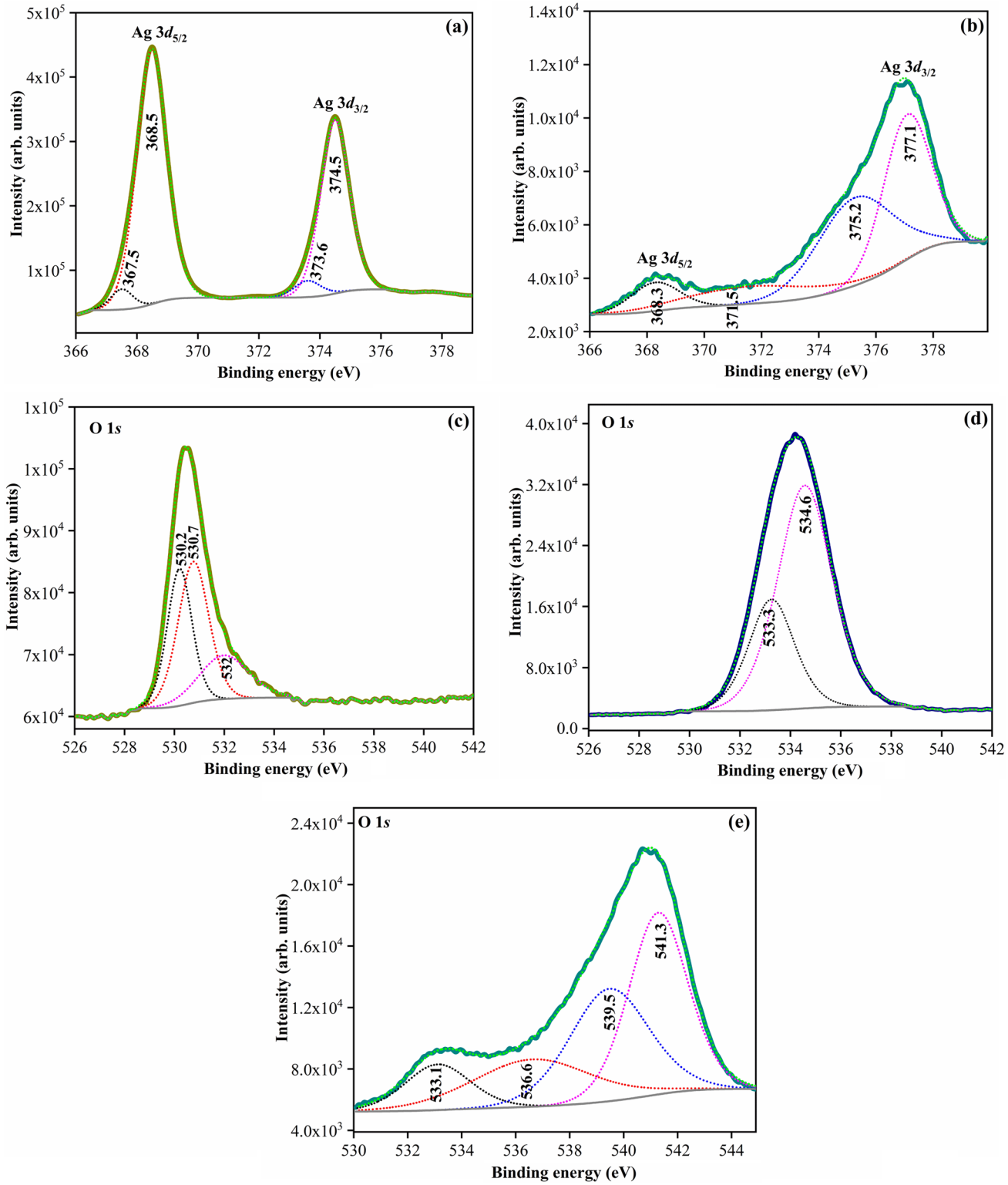

Fig. 8 XPS spectra of Ag 3d of **a** α-Ag_2WO_4 nanocrystals and **b** α-Ag_2WO_4/SBA-15 nanocomposite; XPS spectra of O 1 s of **c** α-Ag_2WO_4 nanocrystals, **d** SBA-15 molecular sieve, and **e** α-Ag_2WO_4/SBA-15 nanocomposite

by an internal electron is increased; thus, an increase in the energies of bonds occurs [105]. Therefore, an increase in the number of different environment of chemical environments, as shown by XPS peak deconvolutions (i.e. chemical shifts), and the interactions between the Si, O, Ag, and W atoms are consistent with the deposition of α-Ag_2WO_4 nanocrystals on the surface of SBA-15 molecular sieve. Peaks assigned to O–H bonds in α-Ag_2WO_4/SBA-15 may be due to Ag–OH bonds and H_2O molecules chemisorbed onto surface defects in the crystal [3, 106]. The presence of O–H groups can be related to defects in the surface of materials promoted by the *in-situ* sonochemical impregnation method [106]. The XPS spectrum of the O-1 *s* orbital for α-Ag_2WO_4/SBA-15 suggests that the in-situ sonochemical impregnation method promoted chemical interactions between Ag present in α-Ag_2WO_4 nanocrystal and O atoms present in SBA-15 molecular sieve. These results are consistent with the profile of the XPS spectra of the 3*d* orbitals for Ag. Hence, the XPS results are consistent with the formation of α-Ag_2WO_4, SBA-15, α-Ag_2WO_4/SBA-15, and the formation of metallic silver in XPS analysis due to X-ray irradiation in the samples.

3.8 RhB Adsorption Study

The adsorption capacity (Q_e, mg g^{-1}) as a function of time (Fig. 9a) shows that adsorbents α-Ag_2WO_4 and α-Ag_2WO_4/SBA-15 have higher adsorption capacity than SBA-15. The adsorption process starts quickly and reaches equilibrium within 15 min. Equilibrium time is in agreement with other RhB adsorption studies reported in the literature [4, 57, 60]. The performance of α-Ag_2WO_4 and α-Ag_2WO_4/SBA-15 are similar, and far superior to that of SBA-15. This suggests that the active sites from α-Ag_2WO_4 determine adsorption performance, leading to the order of performance: α-Ag_2WO_4 > α-Ag_2WO_4/SBA-15 > SBA-15. A probable justification for the low adsorption capacity for SBA-15, despite its high surface area and pore diameter, could be due to a competition between water molecules and RhB to access the negative surface of the isolated silanols in SBA-15, and by repulsion between positive group of RhB ($–N^+$) and groups protonated with adsorbed water (partial charged positive). The SBA-15 has two types of surface silanols: isolated (pKa ~ 2) and geminal (pKa ~ 8.2). In fused silica, an estimated 20% of surface silanols are isolated type and are deprotonated in pH > 2 [96, 107]. Thus, SBA-15 has 20% of surface silanols deprotonated (negative) and 80% of surface silanols protonated. The protonated groups can form hydrogen bonds with H_2O or RhB molecules of carboxylic (COOH) groups; however, water molecules must prevail and the positive partial charge can cause repulsion of positive RhB ($–N^+$) groups. Then, the competition occurs between attractive and repulsive forces, but the repulsive forces prevail justifying low adsorption of RhB on SBA-15, because the positive RhB ($–N^+$) group can be attracted and repelled, respectively, by about 20% of deprotonated silanol groups and about of 80% of protonated groups with water adsorbed (partial charged positive).

Figure 9b shows that the plot Q_e (mg g^{-1}) versus equilibrium concentration (C_e mg L^{-1}) produces concave isotherms, which indicates an extremely favorable process and that the adsorption capacity is high even under conditions of low dye concentrations [108]. These isotherms correspond to Langmuir isotherms with R_L values in the range 0 to 1,

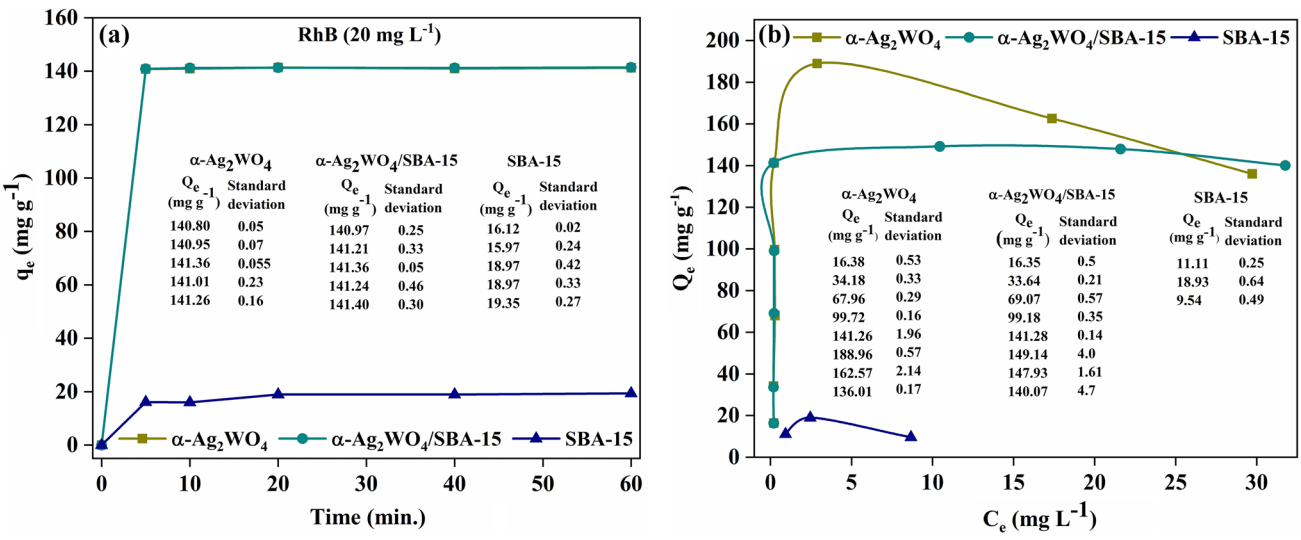

Fig. 9 **a** Adsorption capacity as a function of time and **b** Adsorption capacity as a function of equilibrium concentration for adsorption of RhB on α-Ag_2WO_4, SBA-15, and α-Ag_2WO_4/SBA-15

compatible with a favorable process. In Fig. 9a, b, the inset of standard deviation of measures are all small and with acceptable error (less than 5%).

Adsorption capacity and adsorbent efficiencies of α-Ag_2WO_4, SBA-15, and α-Ag_2WO_4/SBA-15 for the RhB dye are provided in Table 3.

All adsorbents have similar performance at low dye concentration (2.5 mg L^{-1}). This relates to the saturation capacity of available active sites, since at low concentrations (2.5 mg L^{-1}), there are fewer dye molecules in the medium to be adsorbed. This result indicates that the adsorbents are very selective as even at low dye concentrations the adsorption process was satisfactory. The increase in adsorption capacity of α-Ag_2WO_4 and α-Ag_2WO_4/SBA-15 adsorbents is proportional to the initial dye concentration (5, 10, 15, and 20 mg L^{-1}). However, this trend is not observed with SBA-15 at concentrations greater than 2.5 mg L^{-1}. This low SBA-15 performance was not expected due to its high specific area. Beyond the interactions of silanols groups, more explanation of this behavior may be obtained by investigating the thermodynamic properties of its adsorption process. α-Ag_2WO_4 and α-Ag_2WO_4/SBA-15 have high RhB removal efficiency, reaching 99% efficiency at 20 mg L^{-1} RhB concentration. SBA-15 has an efficiency higher than 50%, at low dye concentrations, but is less than 14% efficient at RhB concentrations (10, 15, and 20 mg L^{-1}).

3.9 Adsorption Kinetics and Isotherms

Kinetic study and adjustment of adsorption data to the Langmuir, Freundlich, and Temkin models may provide important information for understanding the mechanism of adsorption. The kinetic study was limited to two kinetic models: pseudo-first order and pseudo-second order. In fitting the pseudo first-order model to experimental data, R^2 values were low (supporting material, Figs. S1 (a–c)). The calculated Q_e from graph values are quite different from the experimental values; therefore, the pseudo first-order model clearly does not fit the RhB adsorption process [60, 109, 110].

The second order rate law (Eq. 7) is adopted in supporting material (Figs. S2 (d–f)). All adsorbents yielded near unit regression coefficients ($R^2 \cong 1$) and good agreement between calculated Q_e a110nd experimental data. Thus, the kinetics of RhB adsorption process with α-Ag_2WO_4, SBA-15, and α-Ag_2WO_4/SBA-15 adsorbents follows pseudo-second order [60, 109,]. Other RhB adsorption studies over different adsorbents have also fitted pseudo-second order kinetics [56, 57, 60, 66, 111, 112]. This model indicates that the adsorption mechanism of the adsorbent is the main factor that interferes with the adsorption capacity. Therefore, RhB removal from solutions is due to physicochemical interactions between the two phases; the rate limiting step should be attributed to chemical adsorption, which may involve valence forces by sharing or exchanging electrons between adsorbate and adsorbent [72, 73, 112]. This takes into account chemical adsorption; however, the negative charge of the adsorbents, as showed by Zeta potential, the positive charge of RhB cationic dye, and the rapidity of the process indicate that the predominant adsorption type is not chemical.

The Langmuir model is a linear model. Following Eq. 3, plotting (C_e/q_e) versus (C_e) gives the parameters: Q_{max} (maximum adsorption capacity, mg g^{-1}), K_L (adsorption energy constant, L mg^{-1}), and R^2 (R squared, regression coefficient). Supporting material Fig. S2 (a–c) shows that for all adsorbents $R^2 \cong 1$. Hence adsorption of RhB by α-Ag_2WO_4, SBA-15, and α-Ag_2WO_4/SBA-15 fits the Langmuir Model [57, 60, 66].

The values of q_e from the model are close to the experimentally obtained q_e. This means that adsorption occurs as a monolayer at specific adsorbent sites and that there is no interaction between the adsorbate molecules [57, 60, 66]. This is consistent with previous investigations of RhB adsorption on various materials, such as beta zeolite, graphene oxide composite/beta zeolite, and Zn /Co-ZIF. Adsorption of RhB by these materials also fit the Langmuir model [57, 60, 66].

The process may be favorable or unfavorable, which can be verified by the R_L value (Eq. 4) from the Langmuir model. Supporting material Fig. S2 (a–c) demonstrate that the R_L is between 0 and 1 ($0 < R_L < 1$) for the three adsorbents. This indicates that the process is favorable and is consistent with the isotherm obtained based on Q_e versus C_e, as already indicated in Fig. 10b.

In the Freundlich model (supporting material Fig. S3 (a–c)), all adsorbents yielded relatively low R^2, and there was no correlation between the Q_e values calculated from

Table 3 Adsorption capacity and efficiency of adsorbents for the RhB dye

Q_e (mg g^{-1})					
Adsorbents	Concentration (mg L^{-1})				
	2.5	5.0	10	15	20
SBA-15	11.2	17.5	11.4	12.5	19.4
α-Ag_2WO_4	16.4	34.2	68.8	105.5	142.0
α-Ag_2WO_4/SBA-15	17.1	33.9	69.3	105.6	141.8
Adsorbent efficiency (η)					
SBA-15	63.2%	54.8%	12.52%	11.7%	13.5%
α-Ag_2WO_4	91.8%	96.2%	98.0%	98.2%	99.1%
α-Ag_2WO_4SBA-15	94.4%	96.9%	98.1%	98.3%	98.7%

$\eta = \frac{(C0-Ce)x100}{C0}$ where C_0 and C_e are initial concentration and dye equilibrium concentration (mg L^{-1}), respectively

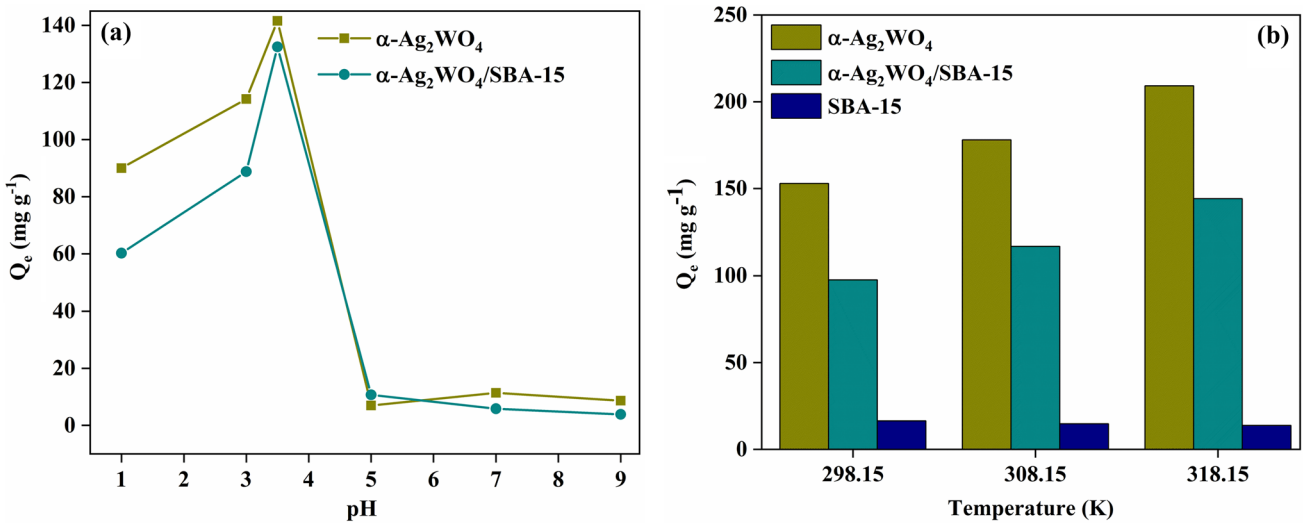

Fig. 10 **a** Influence of pH in adsorption capacity of RhB on α-Ag_2WO_4 and α-Ag_2WO_4/SBA-15 and **b** influence of temperature in adsorption capacity of RhB on α-Ag_2WO_4, SBA-15, and α-Ag_2WO_4/SBA-15

the model and experimental values. Hence, this model does not fit the RhB adsorption process on α-Ag_2WO_4, SBA-15, and α-Ag_2WO_4/SBA-15 [57, 66, 109]. Freundlich model generally fits non-ideal systems, heterogeneous surface, and multilayer adsorption [109].

For the Temkin model (supporting material, Fig. S3 (d–f)), R^2 values are also quite low, indicating that the RhB adsorption study on α-Ag_2WO_4, SBA-15, and α-Ag_2WO_4/SBA-15 does not fit this model. This model is based on the adsorbent-adsorbent interaction and uniform distribution of binding energy and is more suited to processes involving adsorption of gases, since it was initially proposed to describe hydrogen adsorption on platinum electrodes in acidic medium [109].

The maximum adsorption capacity was extracted from Langmuir isotherm. The Maximum adsorption capacities of several adsorbents for RhB are listed in Table 4. α-Ag_2WO_4 and α-Ag_2WO_4/SBA-15 have similar adsorption capacity around 150 mg g^{-1}. This performance is superior to that of many adsorbents and close to the best performing RhB adsorbents that have been reported in recent literature, as shown by Table 4.

Table 4 Comparison of the adsorption capacities of various adsorbents for RhB

Adsorbents	[a]Q_m (mg g^{-1})	pH	Reference
α-Ag_2WO_4/SBA-15	149.25	3.5	This work
Graphene oxide/Beta zeolite	64.47	3	[80]
Zn/CoZIFs derived carbon	116.2	10	[66]
Gelatin/Activated Carbon (GE/AC)	256.41	4	[73]
Exhausted coffee ground powder	5.26	2	[74]
Graphene oxide (GO)/silicalite-1	56.55	3	[111]
SnS_2	200.00	–	[116]
Carbon nanotubes	25.55	–	[61]
perovskite oxide/carbon fibers (LFO-ACFs)	182.6	–	[113]
Beta Zeolites	27.97	3	[57]

[a]Q_m the maximum adsorption capacity

3.10 pH and Temperature Effects

The structure of RhB may take the cationic or zwitterionic form (presence of negatively charged groups and positively charged groups). The nature of RhB in solution and the extent, or predominance of the cationic or zwitterion form depend on the pH [77, 109, 113]. RhB is a cationic dye since the aromatic amino acid group dissociates forming a positive charge on nitrogen, but the presence of carboxylic group allows the loss of H, resulting in a pKa of 3.7 [77, 109, 111, 113]. At pH < 3.7, the RhB ion has a positive charge on either nitrogen, and the carboxylic acid group is neutralized (COOH) [77, 110, 112, 113].

Figure 10a shows the influence of pH on the adsorption process; at pH lower than the RhB pKa (pH < 3.7) adsorption is high due to the predominance of the cationic form of RhB attracted by a negative charge on the surface of the adsorbents. Maximum adsorption of RhB has been reported at pH 3–4 [73, 77]. At pH higher than the RhB pKa (pH > 3.7), the adsorption capacity is significantly reduced. At pH 8, complete conversion to the zwitterionic form occurs (nitrogen positive charge and carboxylic oxygen negative charge) [114]. Repulsion between the negative surface of the adsorbent and the negative charge of the dye can explain the reduction of RhB adsorption. The

measurements of zeta potential and the literature support the negative charge of α–Ag_2WO_4 in wide range pH (1–7) [4, 97]. The study of influence of pH suggests that electrostatic interaction, between the negative surface of the adsorbent and the positive charge of the dye, is the determining factor in this adsorption process.

Figure 10b illustrates that higher temperature favors the adsorption process for all adsorbents, except to SBA-15. Hence, the process is exothermic for SBA-15 and endothermic for α-Ag_2WO_4 and α-Ag_2WO_4/SBA-15 in agreement with other RhB adsorption studies reported in literature [60, 66, 73]. The Gibbs energy value is negative, indicating that the process is spontaneous, which is consistent with the isotherms demonstrating that RhB adsorption on the tested adsorbents is favorable. The influence of temperature on the adsorption capacity of α-Ag_2WO_4, SBA-15, and α-Ag_2WO_4/SBA-15 for RhB was investigated to determine the thermodynamic properties of the adsorption process. Thermodynamic parameters at temperatures of 298.15, 308.15, and 318.15 K are in Table 5. The graphs (ln K as a function of T^{-1}) used to obtain parameters ΔH° and ΔS° are shown in supporting material Fig. S4.

The values of ΔH° and ΔS° (Table 5) are positive for α-Ag_2WO_4 and α-Ag_2WO_4/SBA-15 adsorbents, which corresponds to a reversible endothermic process [74]. The ΔH° and ΔS° values for SBA-15 are negative, indicating that RhB adsorption on SBA-15 is an exothermic process, and the randomness at solid–liquid interface decreased during the adsorption process [77].

The Gibbs energy (Table 5) becomes more negative with increasing temperature for adsorbents α-Ag_2WO_4 and α-Ag_2WO_4/SBA-15. This may be related to the increase of species mobility in solution and/or activation of active sites [71, 73]. The values of ΔH°, ΔS° are positive and ΔG° negative, this indicate spontaneity and reversibility for the process [74]. Thermodynamic parameters for α-Ag_2WO_4 are higher than for α-Ag_2WO_4/SBA-15. This may be related to the density of active sites, since in the proportion of silver tungstate is lower in α-Ag_2WO_4/SBA-15 than in the pure α-Ag_2WO_4 nanocrystals.

For SBA-15, the Gibbs energy (Table 5) becomes less negative with temperature increase, which means that RhB adsorption on SBA-15 is less favorable with increased temperature. The combination of values ΔG°, ΔH°, and ΔS° for SBA-15 clarify the lower adsorption capacity to RhB. However, SBA-15 can facilitate separation between adsorbent and dye solution, and the high specific area dispersed α-Ag_2WO_4 nanocrystals may be added to improve it, as demonstrated by the good performance of α-Ag_2WO_4/SBA-15.

3.11 Effect of Adsorbent Dosage

The relationship between adsorption capacity and adsorbent dosage is relevant for practical applications [115]. Figure 11a shows that the dosage of 0.352 g L^{-1} of both adsorbents, α-Ag_2WO_4 and α-Ag_2WO_4/SBA-15, has removal efficiency of 100% for RhB 50 ppm. This reinforces that the SBA-15 support improves the adsorption capacity of α-Ag_2WO_4 / SBA-15, since even with less active sites (α-Ag_2WO_4) than the pure α-Ag_2WO_4, its adsorption capacity was similar to the last one.

3.12 RhB Desorption from α-Ag_2WO_4 and α-Ag_2WO_4/SBA-15

The desorption of RhB from α-Ag_2WO_4 and α-Ag_2WO_4/SBA-15 by changing pH was efficient and fast. Figure 11b illustrates that at pH 7 the recuperation of Rhb was 80% for α-Ag_2WO_4 and α-Ag_2WO_4/SBA-15. Furthermore, RhB recuperation increased with pH, indicating that dye adsorption on adsorbents is driven mainly by electrostatic forces. As discussed beforehand, in neutral and alkaline pH, RhB takes the zwitterionic form, promoting the repulsion between the charge negatives of RhB and both α-Ag_2WO_4 and α-Ag_2WO_4/SBA-15 [77, 110, 113].

3.13 Mechanistic Pathway

In supporting material, Fig. S5 is a scheme illustrating the main steps of possible mechanism for RhB adsorption on α-Ag_2WO_4, SBA-15, and α-Ag_2WO_4/SBA-15 adsorbents. The mechanism considers that the electrostatic interaction between RhB positive charges (cationic form) and surface negative charge (WO_4^{2-}) of adsorbents dominates the mechanism [4]. The enthalpy values (ΔH° < 40, 34.32 and 26.83 kJ mol^{-1} for α-Ag_2WO_4 and α-Ag_2WO_4/SBA-15,

Table 5 Thermodynamic parameters obtained for rhodamine B adsorption by adsorbents at 298.15, 308.15, and 318.15 K

Adsorbents	Thermodynamics parameters				
	ΔH° (KJ/ mol)	ΔS° (J/ mol K)	ΔG° (KJ / mol)		
			298.15 K	308.15 K	318.15 K
SBA-15	−8.7	−23.03	−1.9	−1.6	−1.4
α-Ag_2WO_4	34.3	132.2	−5.2	−6.3	−7.8
α-Ag_2WO_4/SBA-15	26.8	100.5	−3.2	−4.1	−5.2

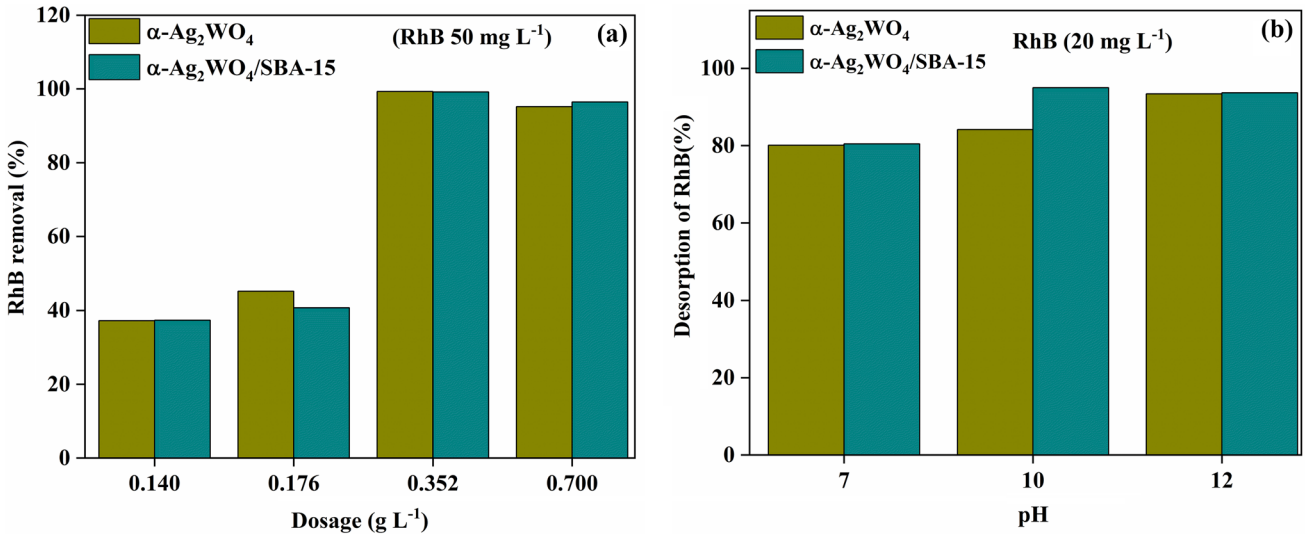

Fig. 11 **a** Effect of sorbent dosage on the adsorption capacity of RhB on α-Ag_2WO_4 and α-Ag_2WO_4/SBA-15 and **b** Desorption of RhB from α-Ag_2WO_4 and α-Ag_2WO_4/SBA-15 by changes of pH

respectively) and kinetics of adsorption are consistent with physical adsorption. In α-Ag_2WO_4, WO_4^{2-} (doubly charged) groups attract selectively and strongly RhB molecules by the positively charged group ($-N^+$) of dye. The carboxylic group can form hydrogen bond with the tungstate unit of α-Ag_2WO_4 [4]. For SBA-15 see explication in item 3.8 about lower adsorption capacity of RhB on SBA-15. In the α-Ag_2WO_4/SBA-15, the groups WO_4^{2-} (doubly charged) disperse on the surface of SBA-15, selectively and strongly attracted RhB molecules by positively charged ($-N^+$) groups, overcoming the repulsion between ($-N^+$) of RhB and protonated ($Si(OH)_2$ groups on the surface of SBA-15 with adsorbed water (partial charged positive). Other interactions may occur, but here they are not determinants of the RhB adsorption process. For example: the pores of SBA-15 can facilitate the entry of bulky RhB molecules with dimensions about of 1.44 nm × 1.09 nm × 0.64 nm [66]; however, significant interactions are unlikely owing to the absence of active sites to maintain the adsorbed RhB molecule. Therefore, the predominant step of mechanism is the electrostatic interaction between the adsorbent WO_4^{2-} negative groups and the positive ($-N^+$) dye charge. Thus, with zwitterionic species (pH > 3.7, the zwitterionic form prevail), the repulsions of the WO_4^{2-} groups with the COO– groups prevail, justifying low adsorption in pH > 3.7.

4 Conclusions

α-Ag_2WO_4 nanocrystals were synthesized with success by a sonochemical method at room temperature with the use of citric acid as chelating agent. The deposition of α-Ag_2WO_4 nanocrystals on the SBA-15 molecular sieve were obtained by in-situ sonochemical methods without modifying the structures of α-Ag_2WO_4 nanocrystals, and the SBA-15 molecular sieve. α-Ag_2WO_4/SBA-15 had textural properties similar to pure SBA-15. X-ray diffraction, Rietveld refinement, micro-Raman, FT-IR, and FE-SEM images indicated that the textural properties are consistent with the deposition of α-Ag_2WO_4 nanocrystals on the external surface of SBA-15. The average pore diameter of α-Ag_2WO4/SBA-15 is larger than that of SBA-15, implying that α-Ag_2WO_4 also deposited within the mesopores. Hence the in-situ sonochemical method may promote active sites on the external surface and inside of the SBA-15 mesopores. XPS details are consistent with the formation of α-Ag_2WO_4 nanocrystals, the deposition of α-Ag_2WO_4 nanocrystals on SBA-15, and the formation of metallic silver due to irradiation of X-ray samples. The results of XPS suggest that the presence of the support can minimize the formation of metallic silver in α-Ag_2WO_4 nanocrystals when irradiated with X-rays. The high-resolution spectrum of O1-*s* orbitals suggest that the sonochemical impregnation method can generate defects in the Ag_2WO_4 nanocrystals deposited in the SBA-15 support (α-Ag_2WO_4/SBA-15). The adsorption behavior of rhodamine B onto α-Ag_2WO_4 nanocrystals, SBA-15, and α-Ag_2WO_4/SBA-15 matched Langmuir adsorption isotherm and pseudo-second-order kinetics. The maximum adsorption capacity of α-Ag_2WO_4/SBA-15 was 150 mg g^{-1} and 99% RhB removal efficiency at 20 mg L^{-1} RhB in 15 min.

The RhB adsorption process on α-Ag_2WO_4 and α-Ag_2WO_4/SBA-15 is pH-dependent, and pH ~ 3.5 is ideal for the process. The thermodynamic parameters showed that the process is endothermic, spontaneous, and compatible

with physical adsorption to α-Ag_2WO_4 and α-Ag_2WO_4/SBA-15. The thermodynamic parameters of SBA-15 indicate that RhB adsorption is less favorable and clarifies the lower performance of pure SBA-15. The main pathway for the adsorption process must be electrostatic interaction between the positive charge of the cationic dye and the negative charges of the adsorbents. Therefore, α-Ag_2WO_4/SBA-15 proved to be a good RhB adsorbent with good adsorptive capacity, fast adsorption/desorption equilibrium time and performance similar to α-Ag_2WO_4 pure nanocrystals, even though it has less dosage of silver tungstate.

Acknowledgements This work was funded by the following Grants – CNPq (455864/2014–4, 307559/2016–8, 305757/2018–0). The authors also wish to acknowledge financial support from the CAPES Institution.

Compliance with Ethical Standards

Conflict of interest All authors declare that they have not conflict of interest.

References

1. C.C. Foggi, M.T. Fabbro, L.P.S. Santos, Y.V.B. de Santana, C.E. Vergani, A.L. Machado, E. Cordoncillo, J. Andrés, E. Longo, Chem. Phys. Lett. **674**, 125 (2017)
2. H. Chen, Y. Xu, Appl. Surf. Sci. **319**, 319 (2014)
3. B.C.H. Ng, W.Y. Fan, CrystEngComm **18**, 8010 (2016)
4. D.P. Dutta, A. Singh, A. Ballal, A.K. Tyagi, Eur. J. Inorg. Chem. **2014**, 5724 (2014)
5. B.-Y. Wang, G.-Y. Zhang, G.-W. Cui, Y.-Y. Xu, Y. Liu, C.-Y. Xing, Inor. Chem. Front. **6**, 209 (2019)
6. R.A. Rocca, J.C. Sczancoski, I.C. Nogueira, M.T. Fabbro, H.C. Alves, L. Gracia, L.P.S. Santos, C.P. de Sousa, J. Andrés, G.E. Luz Jr., E. Longo, L.S. Cavalcante, Catal. Sci. Techonol. **5**, 4091 (2015)
7. N.G. Macedo, A.F. Gouveia, R.A. Roca, M. Assis, L. Gracia, J. Andrés, E.R. Leite, E. Longo, J. Phys. Chem. C **122**, 8667 (2018)
8. V.M. Longo, C.C. de Foggi, M.M. Ferrer, A.F. Gouveia, R.S. André, W. Avansi, C.E. Vergani, A.L. Machado, J. Andrés, L.S. Cavalcante, A.C. Hernandes, E. Longo, J. Phys. Chem. A **118**, 5769 (2014)
9. L.E. da Silva, A.C. Catto, W. Avansi Jr., L.S. Cavalcante, V.R. Mastelaro, J. Andrés, K. Aguir, E. Longo, J. Alloy Compd. **683**, 186 (2016)
10. L.S. Cavalcante, M.A.P. Almeida, W. Avansi Jr., R.L. Tranquilin, E. Longo, N.C. Batista, V.R. Mastelaro, M.S. Li, Inorg. Chem. **51**, 10675 (2012)
11. C. Jiang, J. Liang, Y. Qian, Solution Route to Semiconducting Nanomaterials, Nanocrystalline Materials., ed. By S. C. Tjong (Elsevier Science Ltd, Oxford, 2006) p. 1
12. H. He, S. Xue, Z. Wu, C. Yu, K. Yang, G. Peng, W. Zhou, D. Li, Chinese. J. Catal. **37**, 1841 (2016)
13. K. Vignesh, M. Kang, Mat. Sci. Eng. B **199**, 30 (2015)
14. H. Xu, Y. Cao, J. Xie, J. Hu, Y. Li, D. Jia, Mater. Res. Bull. **102**, 342 (2018)
15. B. Zhu, P. Xia, Y. Li, W. Ho, J. Yu, Appl. Surf. Sci. **39**, 175 (2017)
16. Y. Li, R. Jin, X. Fang, Y. Yang, M. Yang, X. Liu, Y. Xing, S. Song, J. Hazard. Mater. **313**, 219 (2016)
17. Y. Li, Y. Li, S. Ma, P. Wang, Q. Hou, J. Han, S. Zhan, J. Hazard. Mater. **338**, 33 (2017)
18. Y.Y. Lee, H.S. Jung, J.M. Kim, Y.T. Kang, Appl. Catal. B-Environ. **224**, 594 (2018)
19. K.H. Chung, S. Jeong, B.-J. Kim, K.-H. An, Y.-K. Park, S.-C. Jung, Int. J. Hydrogen Energ. **43**, 5873 (2018)
20. K.H. Chung, S. Jeong, B.-J. Kim, K.-H. An, Y.-K. Park, S.-C. Jung, Int. J. Hydrog. Energy **43**, 11422 (2018)
21. S. Silvestre, B. Hennemann, N. Zanatta, E.L. Foleto, Water Air Soil. Pollut. **229**, 40 (2018)
22. F.F.A. Aziz, A.A. Jalil, S. Triwahvono, M. Mohamed, Appl. Surf. Sci. **455**, 84 (2018)
23. T. Jiang, M. Fang, Y. Li, Q. Zhao, L. Dai, J. Taiwan Inst. Chem. E. **80**, 1031 (2017)
24. P. Lu, Z. Qu, Q. Wang, Y. Yuan, E. Cheng, M. Zhao, J. Inorg. Organomet. Polym. Mater. **29**, 2116 (2019)
25. S.A.A. Vandarkuzhali, B. Viswanathan, M.P. Pachamuthu, S.C. Kishore, J. Inorg. Organomet. Polym. Mater. **30**, 359 (2020)
26. L. Zhang, L. Xiao, Y. Zhang, L.J. France, Y. Yu, J. Long, D. Guo, X. Li, Energy Fuels **32**, 678 (2018)
27. A. F. Soares Filho, J. F. Cruz Filho, M. S. Lima, L. M. Carvalho, L. K. R. Silva, J. S. Costa, T. C. M. Dantas, G. E. Luz Jr, Water Air Soil Pollut 229, 268 (2018)
28. K.G. Vibulyaseak, S.B. Deepracha, M. Ogawa, J. Solid State Chem **270**, 162 (2019)
29. L.V. de Souza, O. Tkachenko, B.N. Cardoso, T.M. Pizzolato, S.L.P. Dias, M.A.Z. Vasconcellos, L.T. Arenas, T.M.H. Costa, C.C. Moro, E.V. Benvenutti, Micropor. Mesopor. Mat. **287**, 203 (2019)
30. Y. Y. Lee, H. S. Jung, Y. T. Kang, J. CO_2 Util. 20, 163 (2017)
31. L. Yu, X. Yang, D. Wang, J. Colloid Interface. Sci. **448**, 525 (2018)
32. P. Devi, U. Das, A.K. Dalai, Chem. Eng. J. **346**, 477 (2018)
33. G. Shi. Y. Bao, B. Chen, J. Xu, Reac. Kinet. Mech. 122, 289 (2017)
34. C.R. Patil, C.V. Rode, Fuel **2017**, 38 (2018)
35. J. Wang, C. Liu, S. Yang, X. Lin, W. Shi, J. Phys. Chem. Solids. **136**, 109164 (2020)
36. W. Shi, C. Liu, M. Li, X. Lin, F. Guo, J. Shi, J. Hazard. Mater. https://doi.org/10.1016/j.jharmat.2019.121902
37. X. Lin, C. Liu, J. Wang, S. Yang, J. Shi, Y. Hong, Sep. Purif. Technol. **226**, 117 (2019)
38. W. Shi, M. Li, X. Huang, H. Ren, C. Yan, F. Guo, Chem. Eng. J. **382**, 122960 (2020)
39. W. Shi, H. Ren, M. Li, K. Shu, Y. Xu, C. Han, Y. Tang, Chem. Eng. J. **382**, 122876 (2020)
40. Y. Fang, Y. Cao, Q. Chen, Ceram. Int. **45**, 22298 (2019)
41. A. Sreedevi, K.P. Vattappalam, T. Varghese, J. Electron. Mater. **47**, 6328 (2018)
42. E. Longo, L.S. Cavalcante, D.P. Volanti, A.F. Gouveia, V.M. Longo, J.A. Varela, M.O. Orlandi, J. Andrés, Sci. Rep-UK **3**, 1 (2013)
43. S. Jeong, K.-H. Chung, H. Lee, H. Park, K.-J. Jeon, Y.-K. Park, S.-C. Jung, Int. J. Hydrog. Energy **42**, 17386 (2017)
44. A. Sreedevi, K.P. Priyanka, K.K. Babitha, S.I. Sankararaman, T. Varghese, Eur. Phys. J. B. **90**, 102 (2017)
45. A. Sreedevi, K.P. Priyanka, K.K. Babitha, S. Ganesh, T. Varghese, Micron **88**, 1 (2016)
46. J. Andrés, L. Gracia, P. Gonzalez-Navarrete, V.M. Longo, W. Avansi Jr., D.P. Volanti, M.M. Ferrer, P.S. Lemos, F.A.L. Porta, A.C. Hernandes, E. Longo, Sci. Rep-UK **4**, 5391 (2014)
47. D. Zhao, J. Feng, Q. Huo, N. Melosh, G.H. Fredrickson, B.F. Chmelka, G.D. Stucky, Science **279**, 548 (1998)

48. D. Zhao, Q. Huo, J. Feng, B.F. Chmelka, G.D. Stucky, J. Am. Chem. Soc. **120**, 6024 (1996)
49. A. Chirieac, B. Dragoi, A. Ungureanu, C. Ciotonea, I. Mazilu, S. Royer, A.S. Mamede, E. Rombi, I. Ferino, E. Dumitriu, J. Catal. **339**, 270 (2016)
50. S. Singh, R. Kumar, H.D. Setiabudi, S. Nanda, D.V.N. Vo, Appl. Catal. A-Gen. **559**, 57 (2018)
51. F.C.M. Silva, M.J. Costa, L.K.R. Silva, A.M. Batista, G.E. Luz Jr., S.N. Appl, Sci. **1**, 654 (2019). https://doi.org/10.1007/s42452-019-0677-z
52. G.E. Luz Jr., S.H. Lima, A.C.R. Melo, A.S. Araujo, V.J. Fernandes Jr., J. Mater. Sci **45**, 1117 (2010)
53. J. Zhu, T. Wang, X. Xu, P. Xião, J. Li, Appl. Catal. B **130–131**, 197 (2013)
54. M.M. Araújo, L.K.R. Silva, J.C. Sczancoski, M.O. Orlandi, E. Longo, A.G.D. Santos, R.S. Santos, G.E. Luz Jr., L.S. Cavalcante, Appl. Surf. Sci. **389**, 1137 (2016)
55. T. M. S. Costa, M. S. Lima, J. F. Cruz Filho, L. F. Silva, R. S. Santos, G. E Luz Jr., J. Photoch. Photobio. A 364, 461 (2018)
56. W. Hamza, N. Dammak, H.B. Hadjltaiet, M. Eloussaief, M. Benzina, Ecotox. Environ. Safe. **163**, 365 (2018)
57. Z.-L. Cheng, Y.-X. Li, Z. Liu, Ecotox. Environ. Safe. **148**, 585 (2018)
58. S. H. da Silva Filho, P. Vinaches, S. B. C. Pergher, Mater.Lett. 227, 258 (2018)
59. J. Chen, X. Zhu, Food Chem. **200**, 10 (2016)
60. Z.L. Cheng, Y.-X. Li, Z. Liu, J Alloy Compd. **708**, 255 (2017)
61. A.K. Dutta, U.K. Ghorai, K.K. Chattopadhyay, D. Banerjee, Physica E **99**, 6 (2018)
62. Q. Qin, J. Ma, K. Liu, J. Hazard. Mater. **162**, 133 (2009)
63. B. Li, B. Mu, Y. Yang, Bioresource Technol **277**, 157 (2019)
64. B.S.R. Hall, F.H. Allen, I.D. Brown, Acta Cryst. A **47**, 655 (1991)
65. P.P. Kubelka, J. Opt. Soc. Am. **38**(5), 448 (1948)
66. J. Zhang, X. Yan, X. Hu, R. Feng, M. Zhou, Chem. Eng. J. **347**, 640 (2018)
67. I. Langmuir, J. Amer. Chem. Soc. **38**, 1145 (1916)
68. I. Langmuir, J. Amer. Chem. Soc. **40**, 1361 (1918)
69. H. Freundlich, *Colloid and Capillary Chemistry* (Methuen & Co., Ltd., London, 1926), pp. 110–114
70. M.I. Tempkin, V, Pyzhev. Acta Physicochimica **12**, 327 (1940)
71. R. D. Sousa, A. R. Oliveira, J. F. Cruz Filho, T. C. M. Dantas,A. G. D. Santos, V. P. S. Caldeira, G. E. Luz Jr., Water Air Soil Poll. 229, 125 (2018)
72. X. Peng, F. Hu, H. Dai, Q. Xiong, C. Xu, J. Taiwan Inst. Chem. E. **65**, 472 (2016)
73. F. Hayeeye, M. Sattar, W. Chinpa, O. Sirichote, Colloid. Surfaces A **513**, 259 (2017)
74. K. Shen, M.A. Gondal, J. Saudi Chem. Soc. **21**, 120 (2017)
75. S. Lagergren, Zur theorie der sogenannten adsorption geloster stoffe. Kungliga Svenska Vetenskaps-Akademiens. Handlingar **24**, 1–39 (1898)
76. Y.S. Ho, G.K. Mckay, Trans. IChemE **76B**, 183 (1998)
77. A.A. Inyinbor, F.A. Adekola, G.A. Olatunji, S. Afr, J. Chem. **68**, 115 (2015)
78. M. Jin, Z. Guo, Z. Lv, J. Mater. Sci. **54**, 6853 (2019)
79. I.M. El-Nahhal, J.K. Salem, M. Selmane, F.S. Rodeh, H.A. Ebtihan, Chem. Phys. Lett. **667**, 165 (2017)
80. K. Bendahou, L. Cherif, S. Siffert, H.L. Tidahy, H. Benaissa, A. Aboukais, Appl. Catal. A-Gen. **351**, 82 (2008)
81. P.M. Skarstad, S. Geller, Mater. Res. Bull. **10**, 791 (1975)
82. J.Y. Yang, C.M. Zheng, Y.Q. Wang, M.L. Guo, Micropor. Mesopor. Mat. **204**, 58 (2015)
83. P. Wang, B. Huang, X. Qin, X. Zhang, Y. Dai, M.-H. Whangbo, Inorg. Chem. **48**, 10697 (2009)
84. F.X. Nobre, I.S. Bastos, R.O.S. Fontenelle, E.A.A. Júnior, M.L. Takeno, L. Manzato, J.M.E. de Matos, P.P.O. Nogueira, J.F.S. Mendes, W.R. Brito, P.R.C. Couceiro, Ultrason. Sonochem. (2019). https://doi.org/10.1016/j.ultsonch.2019.104620
85. B. H. Toby (2006) Powder Diffr. 21, 67 (2006)
86. C. C. de Foggi, R. C. de Oliveira, M. T. Fabbro, C. E. Vergani, J. Andrés, E. Longo, A. L. Machado, Cryst. Growth Des. **17**, 6239 (2017)
87. X. Fan, J. Li, Z. Zhao, Y. Wei, J. Liu, A. Duan, G. Jiang, RSC Adv. **5**, 28305 (2015)
88. S. Muthamizh, K. Giribabu, R. Suresh, R. Manigandan, S. Munusamy, S.P. Kumar, V. Narayanan, Int. J. Chemtech Res. **6**, 3392 (2014)
89. E. Longo, D.P. Volanti, V.M. Longo, L. Gracia, I.C. Nogueira, M.A.P. Almeida, A.N. Pinheiro, M.M. Ferrer, L.S. Cavalcante, J. Andrés, J. Phys. Chem. A **118**, 1229 (2014)
90. M.S. Asgari, A. Zonouzi, R. Rahimi, M. Rabbani, Orient. J. Chem. **31**, 1537 (2015)
91. M. Selvamani, G. Krishnamoorthy, M. Ramadoss, P.K. Kumar, M. Settu, S. Ranganathan, N. Vengidusamy, Mater. Sci. Eng. C **60**, 109 (2016)
92. M. Thommes, K. Kaneko, A.V. Neimark, J.P. Olivier, F. Rodriguez-Reinoso, J. Rouquerol, K.S.W. Sing, Pure Appl. Chem. **87**, 1051 (2015)
93. Y. Chai, L. Wang, J. Ren, W.L. Dai, Appl. Surf. Sci. **324**, 212 (2015)
94. D. Xu, B. Cheng, S. Cao, J. Yu, Appl. Catal. B: Environ. **164**, 380 (2015)
95. X. Wang, C. Fu, P. Wang, H. Yu, J. Yu, Nanotechnology **24**, 165602 (2013)
96. A. Szewczyk, M. Prokopowicz, W. Sawicki, D. Majda, G. Walker, Micropor. Mesopor. Mat. **274**, 113 (2019)
97. D. Xu, B. Cheng, J. Zhang, W. Wang, J. Yu, W. Ho, J. Mater. Chem. A **3**, 20153 (2015)
98. Q. Fan, P. Li, D. Pan, *Radionuclides sorption on typical clay minerals: Modeling and spectroscopies*, ed by C. Chen (Elsevier, New York, 2019) pp. 1
99. N.F. Andrade Neto, P.M. Oliveira, M.R.D. Bomio, F.V. Motta, Ceram. Int. **45**, 152015 (2019)
100. M. Pirhashemi, A. Habibi-Yangjeh, J. Colloid Interf. Sci. **491**, 216 (2017)
101. J.F. Cruz-Filho, T.M.S. Costa, M.S. Lima, L.J. Silva, R.S. Santos, L.S. Cavalcante, E. Longo, G.E. Luz Jr., J. Photochem. Photobiol. A Chem. **377**, 14 (2019)
102. J. Wisniewska, K. Grzelak, S.P. Huang, I. Sobczak, C.M. Yang, M. Ziolek, Catal. Today (2019). https://doi.org/10.1016/j.cattod.2019.05.012
103. T. Qiang, Y. Song, J. Zhao, J. Li, J. Alloy Compd. **770**, 792 (2019)
104. H. Wen, X. Zhou, Z. Shen, Z. Peng, H. Chen, L. Hao, H. Zhou, Colloid Surface B **181**, 285 (2019)
105. D.P. Woodruff, T.A. Delchar, *Modern Techniques of Surface Science*, 1st edn. (Elsevier, Cambridge, 1986), p. 683
106. X. Zhang, J. Qin, Y. Xue, P. Yu, B. Zhang, L. Wang, R. Liu, Rep-UK **4**, 4596 (2014)
107. J.M. Rosenholm, T. Czuryszkiewicz, F. Kleitz, J.B. Rosenholm, M. Lindén, Langmuir **23**, 4315 (2007)
108. J.F. Duarte-Neto, J.M. Cartaxo, G.A. Neves, R.R. Menezes, Ver. Eletr. Mater. Proc. **9**, 51 (2014)
109. R. F. do Nascimento, A. C. A de Lima, C. B. Vidal, D. Q. Melo, G. S. Raulino, *Adsorção: aspectos teóricos e aplicações ambientais*, (Imprensa Universitária, Fortaleza, (2014) pp. 256
110. P. Wang, M. Cheng, Z. Zhang, J. Saudi Chem. Soc. **18**, 308 (2014)
111. Z.L. Cheng, Y.X. Li, Z. Liu, J. Ind Eng Chem. **55**, 234 (2017)
112. S.L. Hu, S.Y. Yong, C.L. Wong, J. Appl. Phycol. **21**, 625 (2009)

113. H. Deng, Z. Mao, H. Xu, L. Zhang, Y. Zhong, X. Sui, Ecotox. Environ. Safe. **168**, 35 (2019)
114. S. Yamaguchi, S. Minbuta, S.; K. Matsui, Colloid. Surf. A 555, 309 (2018)
115. Y. Zhou, J. Lu, Y. Zhou, Y. Liu, Environ. Pollut. **252**, 352 (2019)
116. S. Wang, B. Yang, Y. Liu, J. Colloid Interf. Sci. **507**, 225 (2017)

Publisher's Note Springer Nature remains neutral with regard to jurisdictional claims in published maps and institutional affiliations.